Strain localization and fluid migration from earthquake relocation and seismicity analysis in the western Vosges massif (France)

Jean-Luc Got[(1)], Vadim Monteiller[(1,2)], Jocelyn Guilbert[(3)], David Marsan[(1)], Yves Cansi[(3)], Carole Maillard[(3)] , Jean-Paul Santoire[(3)]

(1) LGIT, Université de Savoie, CNRS, Campus Scientifique, 73376, Le Bourget-du-Lac, France.
(2) DTP, Université Paul Sabatier, CNRS, 14 Av. E. Belin, 31400, Toulouse, France.
(3) LDG, CEA-DAM Ile-de-France, BP12, 91680, Bruyères-le-Châtel, France.

Abstract

Understanding the mechanisms of intraplate earthquakes needs well-documented seismological and geodynamical studies, providing informations for adequate mechanical modelling. We analyzed thoroughly the seismic crisis initiated by the Rambervillers (France) M~5.4 earthquake (February 22th, 2003). This earthquake sequence occurred in the western Vosges massif (France), after the Epinal (1973-74) and Remiremont (1984-85) seismic crisis. We computed the mainshock location and focal mechanism, and the double-difference location of 419 aftershocks, comprising 195 well-recorded similar events of the subsequent seismic crisis. An accurate determination of the mainshock depth (12.5 ± 1.5 km) is obtained from the use of pP phases recorded at remote dense seismic networks and waveform modelling. Focal mechanism computed from regional waveform inversion evidences a N135° ± 10° striking, 45°N ± 15° dipping normal fault plane. Detailed space-time analysis of the crisis shows that two earthquake sequences may be discriminated: a classical mainshock-aftershock sequence, and a secondary earthquake sequence beginning 250 days after the mainshock. More events were recorded during the secondary sequence than during the main sequence. Very few similar events were recorded during the immediate aftershock sequence, although the data were continuously recorded. Double-difference location from travel-time difference shows that immediate, non-similar aftershocks sample a 4 km x 2 km wide

subhorizontal area at about 12 km depth. Similar events were far more numerous during the secondary earthquake sequence. Double-difference relocation of these similar events reveals a N135°, 65°N fault plane compatible with the mainshock source mechanism. During this later sequence, seismicity migrates and oscillates, spanning 2 to 3 km vertically at about 12 km depth, strongly suggesting fluid migration. Normal faulting, subhorizontal faulting and fluid transfer at about 12 km depth may be understood as the response of the crust to flexural stresses induced by the alpine compression – mainshock and post-seismic relaxation, including weakening and collapse of the crust, and fluid transfer.

I Introduction

Intraplate strain localization and earthquake occurrence are less well understood than the strain distribution along plate boundaries, as they exhibit various patterns in limited crustal volumes; their relation to the regional stress field is therefore not straigthforward. Intraplate earthquake swarms may however exhibit locally high seismic rates and comprise intermediate to strong magnitude earthquakes (e.g., New Madrid Seismic Zone, USA, M~8, 1811-1812; Charleston, USA, M~7, 1886; Tang Shan, China, M~7.8, 1976; Ayers Rock, Australia, M~5.8, 1989; Bhuj-Gujarat, India, M~7.5, 2001). They are explained by various mechanisms related to heterogeneities in the stress field or in the strength of the lithosphere (e.g., Sykes, 1978; Campbell, 1978; Hinze et al., 1988; Liu and Zoback, 1997; Kenner and Segall, 2000; Iio and Kobayashi, 2002; Gangopadhyay and Talwani, 2003). In most cases, a few evidences constrain unambiguously the physical mechanism of intraplate earthquakes. In this study we bring some seismological constraints to explain the occurrence of recurrent intraplate earthquakes and seismic crises in the western Vosges massif (France), located westward to the Rhine Graben (Figure 1), a major feature of the European Cenozoic Rift System (Ziegler, 1992; Prodehl et al., 1995). The western Vosges massif (France) experiences a sporadic seismic activity, comprising M~5 mainshocks, recorded since 1962 by the permanent seismic network of LDG-CEA. Seismic activity (Figure 1) has first been recorded near Epinal (1973-74) and Remiremont (1984-85) and more recently, in the Rambervillers region (2003-present). The western Vosges massif is known to have been the probable source of one of the most destructive earthquakes in France, the Remiremont earthquake (1682, intensity VIII MSK, M_l estimated to 5.3 (Lambert, 1997)). This seismic activity is the expression of the tectonic activity of the Vosges massif – Rhine graben system. Rhine graben is part of the rift system which developed during Cenozoic in Central Europe**.** Left-lateral strike-slip on N-S to NE-SW faults drives the deformation of the Vosges massif – Rhine graben area since mid-Pliocene (Abhorner, 1975). Recent seismic activity has developpped along NE-SW earthquake swarms (Remiremont crisis, 1984-85; Haessler and Hoang-Trong, 1985; Plantet et Cansi, 1988), with left-lateral or normal left-lateral strike-slip fault mechanisms, but also along the NW-SE direction (Epinal, 1973-74), with right-lateral strike slip, or inverse fault mechanisms. Focal mechanisms of that region allow to find a regional stress tensor in which the major and minor principal stresses have respectively NW-SE and NE-SW directions (Delouis et al., 1993; Plenefisch and Bonjer, 1997)**.**

Rambervillers M_l ~5.4 RéNaSS (5.9 LDG-CEA; difference in magnitude estimation is due to different attenuation laws) earthquake occurred on February 22th, 2003; it is the first M_l ~5 event occurring in that region since the 1682 Remiremont earthquake. It is also one of the largest earthquakes that have occurred in France in the last 50 years. Preliminary results (Cara et al., 2005) show that mainshock focal mechanism was a normal strike-slip, which is right-lateral on the NW-SE striking, N dipping focal plane.

II Detailed seismological study of the Rambervillers seismic crisis

II.1 Mainshock

Rambervillers M_l ~5.4 mainshock was recorded by 32 stations of the LDG-CEA permanent seismic network, installed throughout France. The mainshock was routinely located (48.33°N, 6.67°E, 10 ± 5 km depth) by inversion of P and S-wave first-arrival times. In this study we first refined the estimation of the mainshock focal mechanism and depth.

Depth of the mainshock was computed from pP phases evidenced by cepstral analysis of the waveforms recorded by four remote, dense, short period seismic arrays located in Mongolia, Nepal, Ivory Coast and Norway. pP phases are reflections at the earth surface of the P first-arrival wavetrain emitted at depth, which is received as a refracted wave at teleseismic distances. In a given velocity model, the time delay between P and pP phases strongly constrains the earthquake depth. Reliable estimates of the P-pP time delay are therefore necessary to really improve the earthquake depth accuracy. They may be obtained through the use of cepstral analysis on waveforms recorded by a remote seismic array. Cepstrum is the Fourier transform of the logarithm of the amplitude spectrum of a signal; it is one of the tools used to find echoes in a signal. Kemerait and Sutton (1982) and Alexander (1996) used cepstrum to detect pP phases. Shumway (1971) represented the mean cepstrum to noise cepstrum ratio – the ratio of two χ^2 distributed random variables, which follows a Fisher distribution- and used F statistic as a detection criterion for the echoes evidenced by cepstral analysis. More recently Bonner et al. (2002) applied this approach to the detection of pP phases using seismic arrays, and shaw that filtering the log spectrum around the dominant frequency of the signal strongly increased the reliability of the F statistic to detect pP phases. We followed this approach and filtered the log spectrum between 0.5 Hz and 4.5 Hz. Cepstra were computed for four remote arrays (Mongolia, Nepal, Ivory Coast, and Norway) and stacked (Figure 2a) to evidence the more significant pP peaks. We finally found a pP-P time delay of 4.2 ± 0.3 s, which corresponds to a depth of 13 ± 1 km for this earthquake, using IASP91 (Kennett and Engdahl, 1991) global 1D velocity model.

Mainshock focal mechanism was computed using the inversion of waveforms recorded from five LDG-CEA three-component long period seismic stations. Sensors were long period LP12-type seismometers, with a flat transfer function from 0.5 to 300 seconds; waveforms were sampled at a 4-Hz sample rate. To allow comparison with synthetic seismograms and inversion, waveforms were first filtered between 10 and 50 seconds. Synthetic seismograms were computed in this spectral band by using the discrete wavenumber method (Bouchon, 1981; Cotton and Coutant, 1997). As mainshock local short-period records provided a ~2-Hz corner frequency, 0.5 s was chosen as the source duration. Propagation was computed in a 1-D velocity model (Table 1). Inversion for determining the optimal source parameters (strike, dip, rake and seismic moment) was performed by minimizing the L1-norm residual variance between the observed and synthetic waveforms using a grid search and a genetic algorithm. Resulting synthetic waveforms show a good fit with the observations (Figure 2b). Strike, dip and rake were respectively found to be 316±10°, 44±15° and –108±10°. The source of the earthquake is therefore a NW-SE normal fault. Computed mainshock seismic moment is 1.7 10^{16} Nm. Waveforms recorded at each of the four distant dense short period seismic arrays (Mongolia, Ivory Coast, Nepal, Norway) were finally modelled and allowed to check the source parameters (Figure 2c). Best modelling was obtained for a depth of 12±1km.

II.2 Aftershocks

The mainshock was followed by numerous aftershocks, comprising 6 M_l~3 earthquakes. About two thousands of them were recorded (2003-present) by the permanent LDG-CEA seismic network, constituted by 42 stations throughout France, whose 7 were located 40 to 120 km and well distributed around the epicentral zone; 80% of the aftershocks were recorded by 4 to 7 stations of the network. Time distribution of the aftershock seismicity approximately follows an Omori law during the first two months. The frequency – magnitude aftershock distribution shows that the maximal LDG magnitude is 3.7, whereas the catalogue reveals to be complete down to magnitude 1.8. Aftershocks were preliminary located as a dense cluster in a volume of several km^3 centered near 48°20'N, 6°40'E, about 40 km North to the nearest station HAU (Haudompre). These locations do not allow to represent accurately the seismogenic structure. We therefore performed the double-difference relocation of these events, first by using their travel-time differences; a more accurate relocation was then performed from the cross-correlation of similar earthquake waveforms. For that purpose, we used the seismic waveforms of that earthquake crisis recorded at a 50-Hz sample rate by the permanent LDG-CEA network, from February 22th, 2003 to the end of 2004.

II.2.1 Preliminary location of aftershocks

In the aim of improving the accuracy of the largest possible number of earthquake locations in the crisis, we first performed a double-difference location using travel-time differences. As no seismic station is located very close to the earthquake swarm, seismic network transfer function may strongly amplify the data standard deviation and induce strong location errors. When time delays are not directly measured from waveform cross-correlation but estimated from the difference of travel-times, would their distribution be gaussian, should the standard deviation of the difference be $\sqrt{2}$ times larger than the standard deviation of the travel times. Actual travel-time pdf (probability density function) being long-tailed ones, the pdf of their difference exhibits even longer tails (it is the convolution of the travel-time pdfs). Travel-time differences are not independent quantities, from one event pair to another, as it is the case for time delays computed from waveform cross-correlation, so that we can not expect averaging of outliers in the double difference process. Whereas the modelling error tends to vanish in the differentiation of travel times (discarding the possibility that the solution depends systematically on the actual set of stations), large outliers may occur in the data. They may strongly perturbate the position of the cost function minimum even when they are relatively unfrequent. It is therefore necessary to take into account the actual distribution of the time difference data, both at the time difference computation step, and during the inversion step.

To discard strong outliers in travel-time differences we performed a two-step median filtering. Recall that for two events *i* and j of relative location vector $\mathbf{r}_{ij}$ located at the hypocentral distance Δ the time delay measured at the station *k* may be expressed as, when the aperture $\frac{\mathbf{r}_{ij}}{\Delta}$ is small,

$$\Delta t_{ij}^{k} = \mathbf{r}_{ij}\mathbf{s}^{k} + \Delta T_{0_{ij}} \qquad (1)$$

where $\mathbf{s}^k$ is the slowness vector at the focal depth of the events *i* and j, and $\Delta T_{0_{ij}}$ is the correction in their origin time difference. In the case where the wave vector set used in the relocation correctly samples the focal sphere centered on the events, $\Delta T_{0_{ij}}$ is the average of the time delays Δt_{ij}^{k} computed for the (*i*,*j*) event pair. To avoid the perturbation due to eventual strong outliers, $\Delta T_{0_{ij}}$ is best estimated using the median of Δt_{ij}^{k}.

Estimating $\Delta T_{0_{ij}}$ allows us to infer the quantity $\Delta \tau_{ij}^{k} = \Delta t_{ij}^{k} - \Delta T_{0_{ij}}$, that is, the time delay due to the difference in event location. $\Delta \tau_{ij}^{k}$ is itself perturbated by outliers; its more robust estimator is the median of its absolute value. The theoretical form of $\Delta \tau_{ij}^{k}$ being a cosine, we estimate the maximum geometrically admissible value taken by $\left|\Delta \tau_{ij}^{k}\right|$ from its median:

$$\max(\left|\Delta \tau_{ij}^{k}\right|) = 2\,\mathrm{median}(\left|\Delta \tau_{ij}^{k}\right|) \qquad (2)$$

$\mathrm{median}(\left|\Delta \tau_{ij}^{k}\right|)$ is the median absolute deviation (MAD) of the time delay $\Delta \tau_{ij}^{k}$.

We therefore discard strong outliers whose values are larger than $C\,\mathrm{median}(\left|\Delta \tau_{ij}^{k}\right|)$, where C is a constant larger than 2 (typically 5). This process allows an efficient a priori detection of outliers in travel-time differences.

Even detecting strong outliers does not imply that the time difference distribution follows a gaussian distribution. We estimated the travel-time difference error probability density by computing, for similar events (see §II.2.2) the difference between the travel-time difference and the corresponding time delay difference. We modelled it as a hyperbolic secant (sech) distribution rather than by a gaussian one (Figure 3); we fitted the travel-time distribution by a sech law with a standard deviation of 0.16 s. In order to take into account this distribution in the double-difference inversion process, we used the bayesian approach followed by Monteiller et al. (2005) to locate the events. Both data and model parameters are considered to be affected by a noise modelled as a random variable. Data follow a sech distribution and model (hypocentral) parameters follow a gaussian one. *A priori* knowledge on the hypocentral parameters is given by their absolute locations and their standard deviation σ_h. As σ_h is not perfectly known, we explored wide intervals (Figure 3b) of its value to optimize the cost function

$$(g(\mathbf{m})\mathbf{-d})^T\mathbf{C_d}^{-1}(g(\mathbf{m})\mathbf{-d}) + (\mathbf{m}\text{-}\mathbf{m}_0)^T\mathbf{C_m}^{-1}(\mathbf{m}\text{-}\mathbf{m}_0) \qquad (3)$$

where **m** is the model, **d** the data, g(**m**) the theoretical travel times, $\mathbf{C_d}$ the data covariance, $\mathbf{m}_0$ and $\mathbf{C_m}$ the *a priori* model and model covariance. This approach (see Monteiller et al., 2005 for details) reveals to be very stable, especially when data are noisy and sparse.

From the initial set of ~2000 events recorded during 2003-2004, we finally selected a set of 419 events in which each pair gave at least 6 non-outlier travel-time differences. We relocated these events using the 1D velocity model of Plantet and Cansi (1988; Table 1) and Monteiller et al. (2005) algorithm. Optimal regularization of the inversion was found for σ_h = 5 km, which is the order of magnitude of the expected uncertainty in the a priori absolute locations.

Results (Figure 4) show that hypocenters are distributed following a complex, though not uncoherent, space-time pattern. A striking feature is that aftershocks following immediately the mainshock (75 events recorded by the LDG-CEA network in the first two days, Figure 4c) mainly occurred on a subhorizontal plane, whereas the seismicity occurring later mainly occurred in a confined volume dipping northward (Figure 4b). Location uncertainties (Figure 4d-e) were computed through an exhaustive computation of the location pdf for each of the events. We computed the pdf for each of the relocated events by calculating the residual standard deviation between theoretical and observed time delays in a 10 km x 10 km x 10 km volume around each event, with a 50-m sampling. We determined the volumes corresponding to a 67% probability (one spatial standard deviation) and determined the tangential ellipsoids (gaussian quadratic model) by computing the eigenvalues and eigenvectors of these volumes. Horizontal uncertainty (average ~250 m) shows that the horizontal extent of the immediate aftershocks is significant; vertical uncertainty is larger (average ~400 m) but does not totally account for the computed vertical component. Athough the confidence volumes evidence the network transfer function, their characteristic dimensions remain moderate and allow to keep a sufficient significance to the horizontal extent of the subhorizontal plane and the vertical northward dipping plane.

Some other representations may be used to illustrate the quality of the result. The internal consistency of the relative position vectors **r** with the set of travel time differences $\Delta\tau_{ij}^{k}$ and the set of wave vectors **s** (*s* being the average slowness at the focal depth considered) may be checked by using a stereogram representing the normalized time difference $\delta_{ij}^{k} = \frac{\Delta\tau_{ij}^{k}}{sr_{ij}}$ as a function of the difference between the directions of **k** and **r**. This plot expresses directly the relation between the data and the model when the aperture $\frac{\mathbf{r}_{ij}}{\Delta}$ is small. It shows (Figure 5) that the relative position of each pair in the cluster is generally consistent with the time difference and ray vectors, and that the average relative position error is limited. This result shows that the double-difference solution is not over-regularized: relative positions of the events are coherent and constrained by the time difference data.

II.2.2 Double-difference location of similar earthquakes

Evidencing systematically sets of similar earthquakes in a cluster needs estimating the similarity of the events. For that purpose, we first computed the generalized coherency matrix (matrix whose each coefficient corresponds to the average coherency between the indexed events). Coherency between two signals is a function of frequency defined as the cross-spectrum normalized by the auto-spectra of each of the signals $x(t)$ and $y(t)$, whose Fourier transforms are $X(f)$ and $Y(f)$:

$$\tilde{C}_{xy}(f) = \frac{\overline{X(f)Y^{*}(f)}}{(\overline{X(f)X^{*}(f)})^{\frac{1}{2}}(\overline{Y(f)Y^{*}(f)})^{\frac{1}{2}}} \qquad (3)$$

where star and bar denote respectively complex conjugation and smoothing. Each of the spectral quantity is smoothed over frequency, as coherency measures the linearity of the filter existing between both signals. Coherency may be viewed as the normalized Fourier transform of a tappered cross-correlation. Coherency is computed from 2.56s signal windows, and smoothed over 9 frequency samples. Signals are iteratively aligned before the final computation of the coherency. Coherency function is first averaged over frequency (3-15 Hz) to estimate the similarity between signals recorded by a given station with one coefficient. It is then averaged over stations that have an averaged coherency coefficient larger than 80%, to estimate the similarity between events by only one coefficient, without pollution of that measure by the coherency computed from unsignificant and noisy record pairs. The result is hereafter referred as average coherency.

We computed the average coherency for each possible event pair comprising to the set of 419 events that was first located (§II.2.1); average was performed over frequency (3-15 Hz) and a minimum of 2 stations. Result of the computation (Figure 6) shows that the distribution of the similarity is not homogeneous with time: similar events are less numerous during the first 75 days following the mainshock than during the remaining of the investigated time period. This feature is not related to a known change in the acquisition system, nor in the event recording procedure. The event set occurring during that 75 day period has a few correlation with the following events and within itself. Otherwise, the coherency matrix shows that similar events are mostly belonging to only one multiplet (set of similar events).

From the generalized coherency matrix, we extracted families of similar events by using Eardley's equivalence class algorithm (Press et al., 1986), and we computed their cardinal for each coherency threshold in the interval [0.8, 1], by step of 0.01. When increasing the multiplet cardinal, average coherency and therefore time delay accuracy decreases, but relocation accuracy increases as the squared root of the number of time delays (Got et al., 1994) -for a homogeneous geometrical distribution of seismic stations and gaussian error in time delays-. We therefore choose the optimal number of events to be located by minimizing a cost function chosen to represent the expected relative location error, expressed as a function of coherency:

$$\frac{1}{\sqrt{n}}\sqrt{\frac{1-C^2(n)}{C^2(n)}} \qquad (4)$$

where C is the averaged coherency coefficient, and n the multiplet cardinal. $\sqrt{\frac{1-C^2(n)}{C^2(n)}}$ is the standard deviation on the cross-spectrum phase, which scales the time delay error.

Plotting this cost function as a function of the multiplet cardinal n shows that it reaches a minimum (Figure 7a). We have chosen to retain one suboptimal family of 195 similar events, which corresponds to a coherency of 92%.

Time delays were computed by the cross-spectral analysis of 2.56s signal windows; the time delay θ is directly derived from the slope of the cross-spectrum phase $\phi(f)$:

$$\theta = \frac{1}{2\pi}\frac{d\phi(f)}{df} \qquad (5)$$

f being the frequency. It is computed through the iterative alignement of the signals; at each step, the weighted linear adjustment of $\phi(f)$ is computed between 3 and 15 Hz, the weight being taken equal to the inverse of the standard deviation of $\phi(f)$. This algorithm provides the maximum-likelihood estimate of the time delay.

A first check of the quality of the time delay measurements was done by computing the closure residual error ε for the station l recording the events i, j and k:

$$\varepsilon = \frac{\Delta t_{ik}^{l} - \left(\Delta t_{ij}^{l} + \Delta t_{jk}^{l}\right)}{3} \qquad (6)$$

where Δt_{ik}^{l} stands for the time delay computed at the station l between the waveforms of the events i and k. Closure error is considered as uniformly distributed across the three pairs of correlated events. It was computed for every possible event triplet (i,j,k) for every recording station. Results (Figure 7b) show that 95% of the closure residual error ε remains lower than 5 ms.

Time delays computed for all possible event pairs were furthermore used for relocating the similar events. Similar event relocation was made using the velocity model proposed by

Plantet and Cansi (1988; Table 1). Typical distance between correlated events being some hundreds of meters, and hypocentral distances being ~50 to 100 km, time delays can not resolve the absolute depths of events better than the 1-km accuracy obtained through the use of the mainshock pP phases or short-period waveform modelling (see e.g., Monteiller et al., 2005). Similar events were therefore relatively relocated using an initial absolute position (depth being equal to 12 km) and a linear double-difference relocation method (Got et al., 1994). Searching for relative positions leads to a well-conditioned undamped inversion, and to a location RMS of 7 milliseconds. We checked the internal consistency of data and computed positions (Figure 8). Relocation reveals (Figure 9) an elongated NW-SE pattern for the relocated cluster (195 events), which dips ~65°NE; average thickness (taken perpendicular to the strike-dip plane) is ~150 m. Along this planar structure hypocenters occupy a 3-km vertical, 1-km horizontal band.

Relative position error (that is, the internal deformation of the relocated cluster) may be estimated by several means. We computed the pdf for each of the relocated events by calculating the residual standard deviation between theoretical and observed time delays in a 10 km x 10 km x 10 km volume around each event, with a 10-m sampling. We determined the volumes corresponding to a 67% probability and determined the tangential ellipsoids by computing the eigenvalues and eigenvectors of these volumes (Figure 9). Ellipsoids are generally elongated with depth, showing that location pdf and error are controlled by the seismic network function. Average relative position error is about 75 m horizontally and 200 m vertically. The time delay standard deviation is less then 5 ms and would cause a ~30 m isotropic location error for ideally distributed stations, comprising nadiral and epicentral stations. Therefore the location error is strongly amplified by the network function. Vertical error however remains less than the vertical extent of the swarm and therefore does not hide its main geometric characteristics.

We checked the fault plane strike and dip by constructing a series of synthetic time delay sets computed for various orientations of the relocated event set, by rotating the events relative to the geometric center of the set. We therefore computed the RMS (residual standard deviation) between observed and synthetic time delays as a function of the fault plane strike and dip, keeping respectively the dip and the strike constant. Computation was carried out on large intervals sampled using one-degree steps, for the set of ray vectors corresponding to the well constrained Plantet and Cansi (1988) 1-D regional velocity model (Figure 10). It shows that, for a given ray vector set, the fault plane strike and dip are constrained with an error smaller than 10 to 15°.

II.2.2 Temporal evolution of the seismicity

Earthquake production rate after a mainshock is described as a function of time by the Omori law :

$$n(t) = \frac{K}{c+t} \qquad (8)$$

where $n(t)$ is the seismicity rate (number of earthquakes by unit of time),
K is an amplitude factor,
c is a time offset from the occurrence of the mainshock.

Omori law may therefore be expressed from the cumulated number of earthquakes $N(t)$:

$$N(t) = K \,\mathrm{Log}(c+t) \qquad (9)$$

Plotting $N(t)$ as a function of Log(t) (Figure 11a) -t being counted in days from the mainshock- for the earthquakes of the Rambervillers crisis recorded up to the end of October 2003 (i.e. during ~20 months) and larger than the completude magnitude of the catalog (M_l ~ 1.8), shows that $N(t)$ does not follow an Omori law during the whole time period. After T_0 + 250, the earthquake rate brutally increases, indicating the beginning of a new sequence; seven M~2.7-3.4 (LDG) earthquakes were actually recorded from T_0 + 250 to T_0 + 264. Events following these seven M~2.7-3.4 events are more numerous than those following the mainshock: 165 M > 1.8 events only were recorded during the 250 days following the mainshock, whereas 236 events (recorded in 200 days) followed the seven 2.7-3.4 event sequence. This feature resists even when using higher magnitude thresholds. Rambervillers crisis is therefore not a simple mainshock-aftershock sequence.

Plotting the occurrence time of the earthquakes as a function of their position (Figure 12) shows that the space-time distribution of the hypocenters is not random: group displacement featuring a time migration appears. The crisis begins at depth in the NW, moving up (~+2km) after T_0 + 200 to the SE, and then down (~-2km) at ~T_0 + 400 to the NW. During this time period, the movement describes an oscillation spanning 2 to 3 km depth, larger than the relative position vertical error (about 200 m). Strikingly T_0 + 250 corresponds to the time where the earthquake rate abruptly changes and where the vertical movement stops and finally inverses (moving up before – down after). Both the seismotectonic context (normal faulting, i.e. local deviatoric tension, regional hydrothermal activity) and this remarkable earthquake space-time distribution may favour a fluid migration conjecture.

III Discussion

Determination of the Rambervillers mainshock position using pP phases and short period waveform modelling, shows that its depth is constrained to be, respectively, 13 ± 1 km and . 12 ± 1 km. Long-period waveform inversion allow the determination of the mainshock focal mechanism to be a ~N135° ± 10° striking, 45° ± 15NE dipping normal fault plane. Double-difference location of the 419 best recorded events of the 2003-2004 Rambervillers seismic crisis shows that most largest immediate aftershocks were located on a subhorizontal plane southward of the mainshock, whereas later seismicity developped along a more steeply northward dipping fault surface, below the mainshock. Search for similar events among these 419 well-recorded events shows that a few of them were similar in the first 75 days following the mainshock. After that time period, seismicity rate increased and recorded similar events were far more numerous. Careful double-difference location of these similar events shows that they occured along a ~N130 ± 10° striking, 65 ± 15° NE dipping fault plane. It is however difficult from these results to conclude whether this plane deduced from aftershock relocation is identical to the mainshock fault plane or not. If we consider that confidence intervals for dip and direction are overlapping and do not allow to discriminate both planes, these fault planes may be gathered in a unique average ~N135° ± 10° striking, ~55°N ± 15° dipping normal fault plane located at ~12.5 ± 1.5 km depth.

After the mainshock, the depth of the seismicity decreased and seismicity followed an Omori law during 75 days. After that date the seismicity rate increased and the seismicity migrated upward. At T_0 + 250 a new sequence began with the occurrence of M~3 events, followed by a brutal increase in the seismicity rate, and the inversion of the movement (seismicity depth finally increases). This pattern may suggest fluid migration. This set of observations has to be compared to other results in the region, in order to understand what are the conditions that favour such a striking seismicity pattern.

Understanding the horizontal development of the seismicity just after the occurrence of a steep dipping normal fault is not straightforward. Despite the care taken in the analysis, one can not totally exclude that (i) the magnitude filtering due to the seismic network grid, (ii) the network transfer function, (iii) the lack of similarity of the recorded immediate aftershocks and (iv) the consequent increase in the location uncertainty may hide the aftershock activity of the mainshock fault plane. However location uncertainty is larger vertically than horizontally and immediate aftershocks were larger and best recorded than the following. The horizontal extent of the immediate aftershock zone is larger than the uncertainties. The vertical extent of the whole set of locations is ~4 km. Figure 5 shows that the time differences, ray vectors and relative positions are coherent. Relative positions are therefore well constrained by the data, and are not over-regularized by the a priori information (σ_h = 5 km). The most likely explanation is that the aftershocks immediately following the mainshock on its rupture plane might be mostly of too weak magnitude to be correctly recorded by the LDG-CEA network (completude magnitude 1.8), and therefore do not belong to our catalog. However, normal faulting and aftershocks occurring on a subhorizontal plane may have a mechanical coherence that we have to investigate.

Microseismicity has already been evidenced in the upper and lower crust in the Vosges and Black Forest massifs (e.g., Delouis et al., 1993; Plenefisch and Bonjer, 1997). Stress tensor in the Black Forest, Vosges and Rhine graben, computed from collections of earthquake focal mechanisms (see e.g. Plenefisch and Bonjer, 1997) shows that major and minor principal stresses σ_1 and σ_3 are horizontal, striking respectively ~N145° and N55° in the upper crust. This stress tensor induces right-lateral strike-slip and normal components on a N135°, 55°N fault plane. In the lower crust, σ_1 is vertical and σ_3 remains N55° striking, horizontal (σ_1 and σ_2 permute). This stress tensor induces normal faulting on a N135°, 55°N fault plane. The Remiremont earthquake (1984, NS left-lateral strike-slip; Haessler and Hoang-Trong, 1985), Epinal (1974) or Rambervillers (2003) earthquakes (NW-SE normal right-lateral strike-slip) are explained by the same stress tensor, working since mid-Miocene (e.g., Villemin et al., 1986).

σ_1-σ_2 permutation with depth and normal faulting at the base of the upper crust and in the lower crust may be examined by looking at the Moho topology in North-East France (Dèzes and Ziegler, 2001; Figure 13a). Continental crust is deeply downward flexured by the Alpine collision: Moho reaches 60 km beneath the Alps, and only 21-22 km beneath the Rhine graben, where it reaches its minimum depth and forms a flexural arch. It recovers its normal depth (down to 35 km) farther in NW France, under the Paris Basin. Moho depth below the western Vosges is about 24 km. Continental crust between western Vosges and Rhine graben is thinned and deformed between the thicker Paris Basin and Alpine foreland. 12-km depth is generally accepted as the brittle/ductile transition in a standard continental crust, that is the upper/lower crust limit (see e.g., Scholz, 1991), where large intraplate earthquakes nucleate. Concavity of the Moho (and continental crust) is directed downward beneath the Rhine graben, and upward in the western Vosges massif. In that context, principal stress permutation may occur when crossing the neutral surface between upper and lower crust near 10-15 km depth; flexural stresses may cause normal faulting in the lower crust beneath the western Vosges massif, whereas strike slip or even thrust faulting occurs in the upper crust. We therefore see that flexural stresses may explain some important features of the regional stress tensor and associated strain.

Flexure of the crust and upward concavity below the western Vosges and normal faulting in the lower crust is summarized in Figure 13. Such a normal fault has finite dimensions and is embedded in the crust whose otherwise global deformation at that time period is aseismic. Therefore the extension occurring in the lower crust is accompanied by contraction in the upper crust: deviatoric stresses accumulate and relax through a necessary subhorizontal differential displacement (readjustment), which may localize at a depth where the deviatoric stress intensity reaches the rock strengh. It provokes the sliding of layers over each other ("layer-over-layer sliding"). It may occur quasi-simultaneously with the normal fault mainshock. Accumulated elastic energy is rapidly relaxed along the normal fault, as (i) rock tensional strength is about ten times lower than its compressive stength, and (ii) tension induces the loss of contact between footwall and hanging wall. Therefore the residual strength of the normal fault is expected to be weak, and its post-seismic relaxation leads to a few stress accumulation and low-magnitude seismicity. In contrast, accompanying subhorizontal readjustments occur along strike-slip faults subject to a strong normal component and should induce larger magnitude aftershocks. Therefore normal fault mainshock and subhorizontal aftershocks may be associated without loss of mechanical significance.

We observed that Rambervillers seismicity occurred in several sequences. After T0+75 the seismicity rate departs from a simple Omori law, then began migrated upward. At T0+250 a new active sequence began migrating downward, along a 3-km high fault plane at about 12-km depth. Upward migration of the seismicity was limited, although sufficient stresses existed to continue a seismic deformation in another direction. Audin et al. (2004) also evidenced that seismicity horizontally migrated along a ~30-km long, but vertically confined 3-km high fault zone during the 1984-85 Remiremont (Vosges, France) seismic crisis. Such a seismic pattern at that scale is significant of a large-scale process and suggests fluid propagation and confining, which may be controlled by the state of stress. This vertical confining is compatible with the local flexure and upward concavity of the crust: horizontal deviatoric stresses are compressive about the neutral surface and tensional below. This stress pattern favours the injection of pressurized fluids at the base of the lower crust and their ascent up to a limited depth in the upper crust. They may propagate horizontally at the top of the tensional zone. This 12-km depth level may trap fluids and be a weak layer, able to favour the develoment of the microseismicity, though there is no pre-existing fault plane. Finally we could conjecture a coherent synthetic mechanical picture explaining the spatio-temporal distribution of the seismicity in that region: due to the action of flexural stresses (induced by the alpine collision), normal faulting and associated layer-on-layer sliding occur; the crust locally weakens and collapses, pressurizing the fluids and provoking their (delayed) ascent up to the base of the upper crust. In that interpretation, fluid transfer would be an evidence of post-seismic relaxation processes, invoking collapse of the crust. Would the long-term migration of seismicity recorded during the 1984-1985 Remiremont crisis (Audin et al., 2005) the evidence of a large-scale, progressive, slow collapse of the crust under flexural stress conditions?

IV Conclusion

The detailed study of the Rambervillers seismic crisis revealed that the mainshock occurred on a N135° ± 10° striking, 45°N ± 15° dipping fault plane, with a normal fault mechanism, at 13 ± 1 km depth. Double-difference relocation shows that the largest immediate (T0 to T0+3) recorded aftershocks occur mainly on a 5 km x 3 km subhorizontal plane. Following aftershocks tend to occur on a N135° ± 10° striking, 65°N ± 15° dipping fault plane, with a normal fault mechanism, at ~12 ± 1.5 km depth. Cross-spectral time delay computation using similar earthquakes allow to compute earthquake locations with an average relative vertical error (~200m) less than the vertical development (3 km) of the seismicity. These locations show that seismicity migrates along the fault plane, first upward up to end-October 2003 (T0 +250), where several M~3 earthquakes occurred; in the following seismic sequence, the movement was reversed and the seismicity propagated downward.

This seismic crisis may be understood from the regional stress tensor (Delouis et al., 1993; Plenefisch and Bonjer, 1997) and the Moho topology in North-East France (Dèzes and Ziegler, 2001). European plate is deeply flexured by the Alpine collision; its concavity is downward beneath the Rhine graben, and upward beneath the western Vosges. Stress tensor shows that contraction occurs locally in the upper crust, whereas tension occurs in the lower crust. This deformation process may induce (i) normal faulting in the lower crust, (ii) subhorizontal readjustments near the neutral surface, and (iii) possible migration of pressurized fluids from depth and storage at the base of the upper crust. These features are compatible with the spatio-temporal distribution of the seismicity. In that context, post-seismic relaxation may be accompanied by the weakening and collapse of the crust, fluid transfer and systematic non-Omori seismicity at the top of the lower crust.

The Remiremont-Epinal-Rambervillers region is an important active and long-lived structural limit, corresponding to a thinned continental crust stressed between two thicker structural domains. It may be a major seismic zone in France. Its stress state could finally favour superficial seismicity that may generate strong ground motions locally. This example may illustrate how intraplate seismic strain may be controlled by the strength of the continental crust, a possible geodynamical process able to generate “low-strength” (Iio and Kobayashi, 2002) class intraplate earthquakes.

Acknowledgements:
This work was carried out in the frame of the LDG-CEA contract #4600101825/P6H53.

REFERENCES

Abhorner, L., Present day stress field and seismotectonic block movements along major fault zones in Central Europe, *Tectonophysics*, 29, 233-249, 1975.

Aki K, Maximum likelihood estimate of b in the formula log N = a - b m and its confidence limits, *Bull. Earthquake Res. Inst.*, Tokyo Univ, 43, 237 – 239, 1965.

Alexander, S.S., A new method for determining source depth from a single regional station, Seism. Res. Lett., 67, 63, 1996.

Audin, L., Avouac, J.-P., Flouzat, M. and J.-L. Plantet, Fluid-driven seismicity in a stable tectonic context: The Remiremont fault zone, Vosges, France, *Geophys. Res. Lett.*, doi 10.1029/2001GL012988, 2002.

Bonner, J.L., Reiter, D.T. and Shumway, R.H., Application of a cepstral *F* statistic for improved depth estimation, *Bull. Seismol. Soc. Am.*, 92, 5, 1675-1693, 2002.

Bouchon, M., A simple method to calculate Green's functions for elastic layered media, *Bull. Seismol. Soc. Am.*, 71, 959-071, 1981.

Campbell, D.L., Investigation of the stress-concentration mechanism for intraplate earthquakes, *Geophys. Res. Lett.*, 5, 477-479, 1978.

Cara, M., W. Brüstle, M. Gisler, P. Kästli, C. Sira, C. Weihermüller and J. Lambert, Transfrontier macroseismic observations of the Ml = 5.4 earthquake of February 22, 2003 at Rambervillers, France, *Journal of Seismology*, 9, 317-328, 2005.

Cotton, F. and O. Coutant, Dynamic stress variations due to shear faults in a plane layered medium, *Geophys. J. Int.*, 128, 676-688, 1997.

Delouis, B., Haessler, H., Cisternas, A. and L. Rivera, Stress tensor determination in France and neighbouring regions, *Tectonophysics,* 221, 413-438, 1993.

Dèzes, P. and P.-A. Ziegler, European Map of the Mohorovicic discontinuity. 2nd EUCOR-URGENT Workshop (Upper Rhine Graben Evolution and Neotectonics), Mt. St. Odile, France, 2001.

Gangopadhyay, A. and P. Talwani, Symptomatic features of intraplate earthquakes, *Seismol. Res. Lett*., 74, 863-883, 2003.

Got, J.-L., J. Fréchet, and F.W. Klein, Deep fault plane geometry inferred from multiplet relative relocation beneath the south flank of Kilauea, *J. Geophys. Res.,* **99**, 15375-15386, 1994.

Haessler, H., and P. Hoang-Trong, La crise sismique de Remiremont (Vosges) de décembre 1984 : Implications tectoniques régionales, *Compte-Rendus de l'Académie des Sciences Paris,* 300, II, 14, 1985.

Hinze, W.J., L.W. Braile, G.R. Keller, and E.G. Lidiak, Models for mid-continent tectonism: An update, Rev. Geophys., 26, 699-717, 1988.

Iio, Y., and Y. Kobayashi, A physical understanding of large intraplate earthquakes, *Earth Planets Space*, 54, 1001-1004, 2002.

Kemerait, R.C., and A.F. Sutton, A multidimensional approach to seismic event depth estimation, *Geoexploration*, 20, 113-130, 1982.

Kenner, S., and P. Segall, A mechanical model for intraplate earthquakes: Application to the New Madrid seismic zone, *Science*, 289, 2329-2332, 2000.

Kennett, B.L.N., and E.R. Engdahl, Travel times for global earthquake location and phase identification, *Geophys. J. Int.*, 105, 429-465.

Lambert, J., Les tremblements de terre en France, mémoire du BRGM, 43-47, 1997.

Liu, L., and M.D. Zoback, Lithospheric strength and intraplate seismicity in the New Madrid seismic zone, Tectonics, 16, 585-595, 1997.

Monteiller, V., Got, J.-L., Virieux, J and P.G. Okubo, An efficient algorithm for double-difference tomography and location in heterogeneous media, with an application to the Kilauea volcano, Hawaii, *J. Geophys. Res.*, 110, B12306, doi:10.1029/2004JB003466, 2005.

Plantet, J.-L. and Y. Cansi, Accurate epicenters location with a large network. Example of the 1984/1985 Remiremont sequence, in Bonnin, J., Cara, M., Cisternas, A. et R. Fantecchi (Editors), *Seismic hazard in Mediterranean regions*, Kleuver, Dordrecht, pp. 347-358, 1988.

Plenefisch, T. and K.-P. Bonjer, The stress field in the Rhine Graben area inferred from earthquake focal mechanisms and estimation of frictional parameters, *Tectonophysics*, 275, 71-97, 1997.

Press, W.H., Teukolsky, S.A, Vetterling, V.T. and B.P. Flannery, *Numerical Recipes: The Art of Scientific Computing*, Cambridge University Press, 518 p., 1986.

Prodehl, C., S. Mueller and V.Haak, The European Cenozoic Rift System, in *Continental Rifts: Evolution, Structure, Tectonics,* K.H. Olsen (Editor), Developments in Geotectonics, vol. 25, Elsevier, Amsterdam, pp. 133-212, 1995.

Scholz, C.H., *The mechanics of earthquakes and faulting*, Cambridge University Press, 471p., 1991.

Shumway, R.H., On detecting a signal in N stationarily correlated noise series, *Technometrics*, 10, 523-534,1971.

Sykes, L.R., Intraplate seismicity, reactivation of preexisting zones of weakness, alkaline magmatism, and other tectonism post-dating continental fragmentation, *Reviews of Geophysics and Space Physics*, 16, 621-688, 1978.

Villemin, T., F. Alvarez, and J. Angelier, The Rhine graben : extension, subsidence, and shoulder uplift, Tectonophysics, 128, 47-59, 1986.

Ziegler, P.A., European Cenozoic Rift System, in *Geodynamics of Rifting, Volume I, Case history studies on rifts: Europe and Asia*, P.A. Ziegler (Editor), Tectonophysics, 208, 91-11, 1992.

TABLE CAPTIONS

Table 1: 1-D regional velocity model used for the earthquake location (Plantet and Cansi, 1988).

FIGURE CAPTIONS

Figure 1 : Simplified structural map of the western Vosges massif (France) showing the earthquake epicenters (solid circles and squares) at the time of the Epinal (1974, red), Remiremont (1984-85, blue) and Rambervillers (2003-2004, yellow) seismic crises, and seismic stations of the LDG-CEA network (black solid triangles). c1, c2: cretaceous; j1, j2, j3: jurassic; t1, t2, t3: triassic; h1, h2, h3: “houiller“ (carboniferous); orange: Vosges granite. Sketch: LDG-CEA seismic network, showing the short period (blue triangles) and the long period (red triangles) stations.

Figure 2: (a) Normalized averaged cepstrum as a function of the pP-P time delay. Cepstrum was averaged over the four remote dense seismic arrays used. (b) Comparison of the long period waveforms observed at regional distance (red) with the waveforms computed using the optimal source parameters (blue). (c) Comparison of the short period waveforms recorded by dense arrays at teleseismic distances (red) with the waveforms computed using the optimal source parameters (blue).

Figure 3 : (a) Probability density function of the travel-time differences; red line: before outlier median filtering; blue line: after outlier median filtering. Modelling of this pdf using (i) a gaussian function (black line), (ii) a sech function (green line). Sech function fits approximately the pdf of the travel-time differences after median filtering.
(b) Cost function and RMS as a function of the a priori standard deviation on the hypocentral position.

Figure 4 : Map (a) and NE-SW vertical cross-section (b) of the hypocenters, showing magnitude and occurrence time of the 419 relocated events. NE-SW vertical cross-section (c) of the first 75 events, occurring during the first two days following the mainshock.

Mainshock is represented at the origin. Map (d) and NE-SW vertical cross-section (e) of the relocated hypocenters (crosses), with their 67% confidence intervals (ellipses, see text for the details of the computation).

Figure 5 : (a) Stereographic plot showing the normalized time difference (see text for details) as a function of the angle (in degrees) between the relative position vector and the ray direction at the focus, for the set of 419 relocated events. The set of ray (slowness) vectors is unique for the whole set of events; the time difference due to the difference in location is the dot product of the relative position vector and the slowness vector (eq. (1)). A polar pattern is observed, which shows that the values of the normalized time delay are coherent with the computed relative positions.
(b) Same representation, for the first 75 events of the sequence, all of them occurring in the first two days following the mainshock and located on a sub-horizontal plane.

Figure 6: Generalized coherency matrix: average coherency coefficient (in percent, color scale) as a function of its two correponding event indices, for the set of 419 events recorded by at least 6 common stations.

Figure 7 : (a) Cost function (eq. 2) as a function of the number *n* of correlated events; (b) Probability density function of the closure residual error ε (eq. 6).

Figure 8 : Stereographic plot showing the normalized time delay (see text and Figure 5 for details) as a function of the angle (in degrees) between the relative position vector and the ray direction at the focus, for the set of 195 similar events.

Figure 9: (a) Map and (b) NE-SW vertical cross-section of the relocated hypocenters of the 195 similar events (crosses), with their 67% confidence intervals (ellipses, see text for the details of the computation). The black solid line in (b) features a 68° dip.

Figure 10 : RMS as a function of fault plane azimuth (a) and dip angles (b), for the Plantet and Cansi (1988) 1-D regional velocity model.

Figure 11 : (a) Cumulated number and cumulative seismic moment of M_l > 1.8 earthquakes as a function of lapse time from the mainshock occurrence, during the Rambervillers seismic

crisis; (b) Blue: magnitude of aftershocks as a function of time after the mainshock; red: completude magnitude computed in 20-event moving windows using Aki's (1965) estimation; black, completude magnitude ($M_c = 1.8$) used for the figure 11a.

Figure 12 : Occurrence time as a function of the relocated earthquake horizontal (a) and vertical (b) position.

Figure 13 : (a) Map of the Moho depth in western Europe (from Dèzes and Ziegler, 2001); (b) schematic SE-NW vertical cross-section of the lithosphere in north-eastern France, showing our interpretation of the deformation process at work in the western Vosges (France).

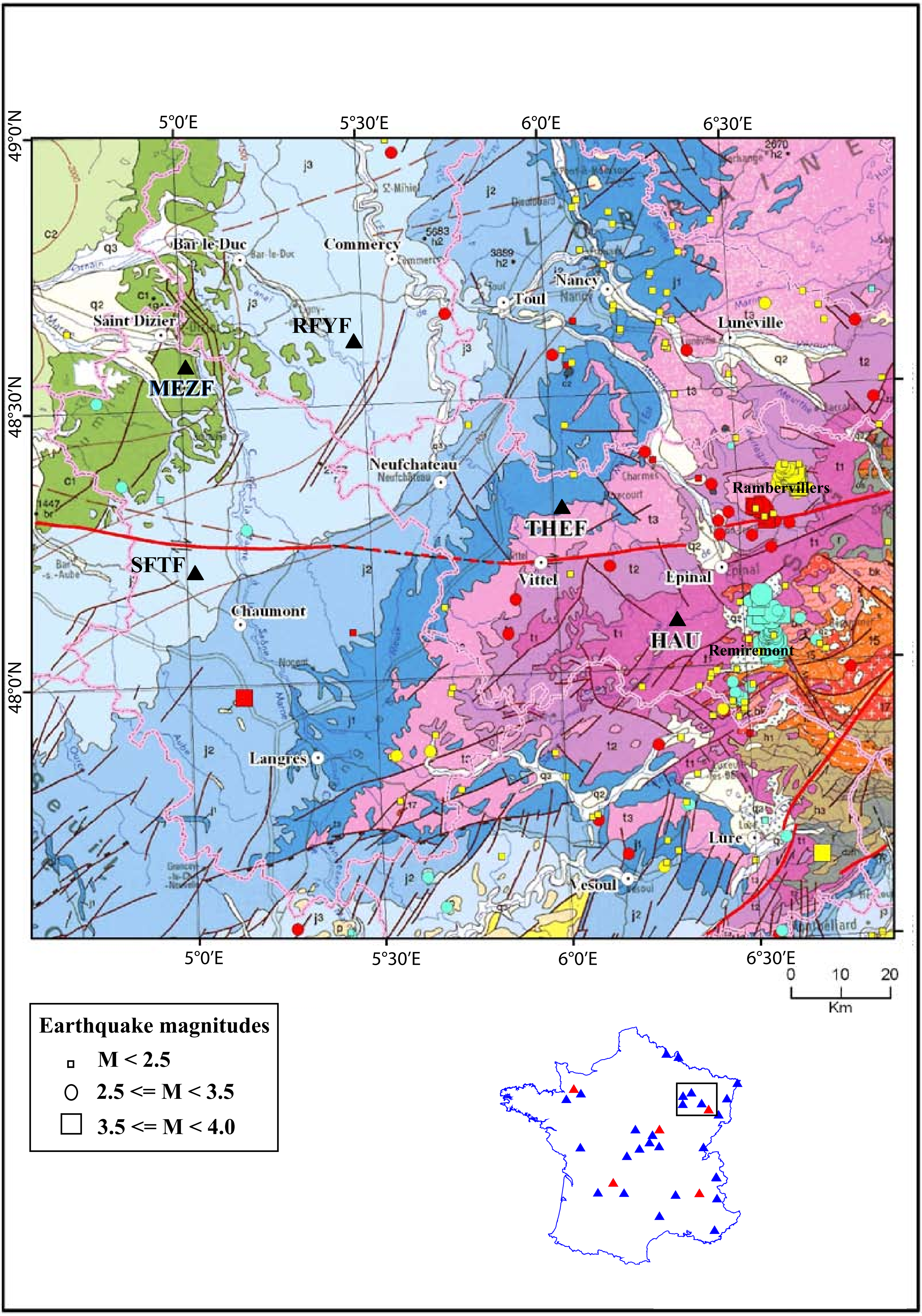
49°0'N
48°30'N
48°0'N
5°0'E
5°30'E
6°0'E
6°30'E
Bar le Duc
Commercy
Nancy
Toul
Saint Dizier
RFYF
Luneville
MEZF
Neufchateau
Rambervillers
THEF
SFTF
Vittel
Epinal
Chaumont
HAU
Remiremont
Langres
Lure
Vesoul
0 10 20
Km
Earthquake magnitudes
M < 2.5
2.5 <= M < 3.5
3.5 <= M < 4.0

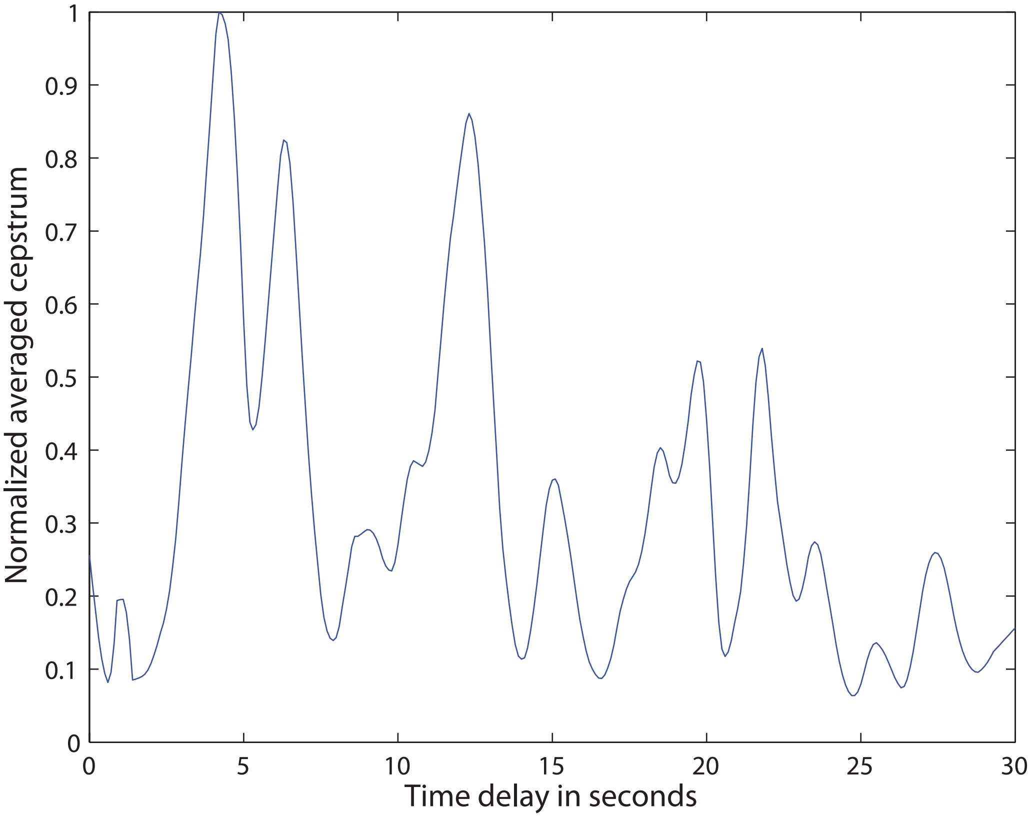
Normalized averaged cepstrum
0
0.1
0.2
0.3
0.4
0.5
0.6
0.7
0.8
0.9
1
0
5
10
15
20
25
30
Time delay in seconds

Figure 2a

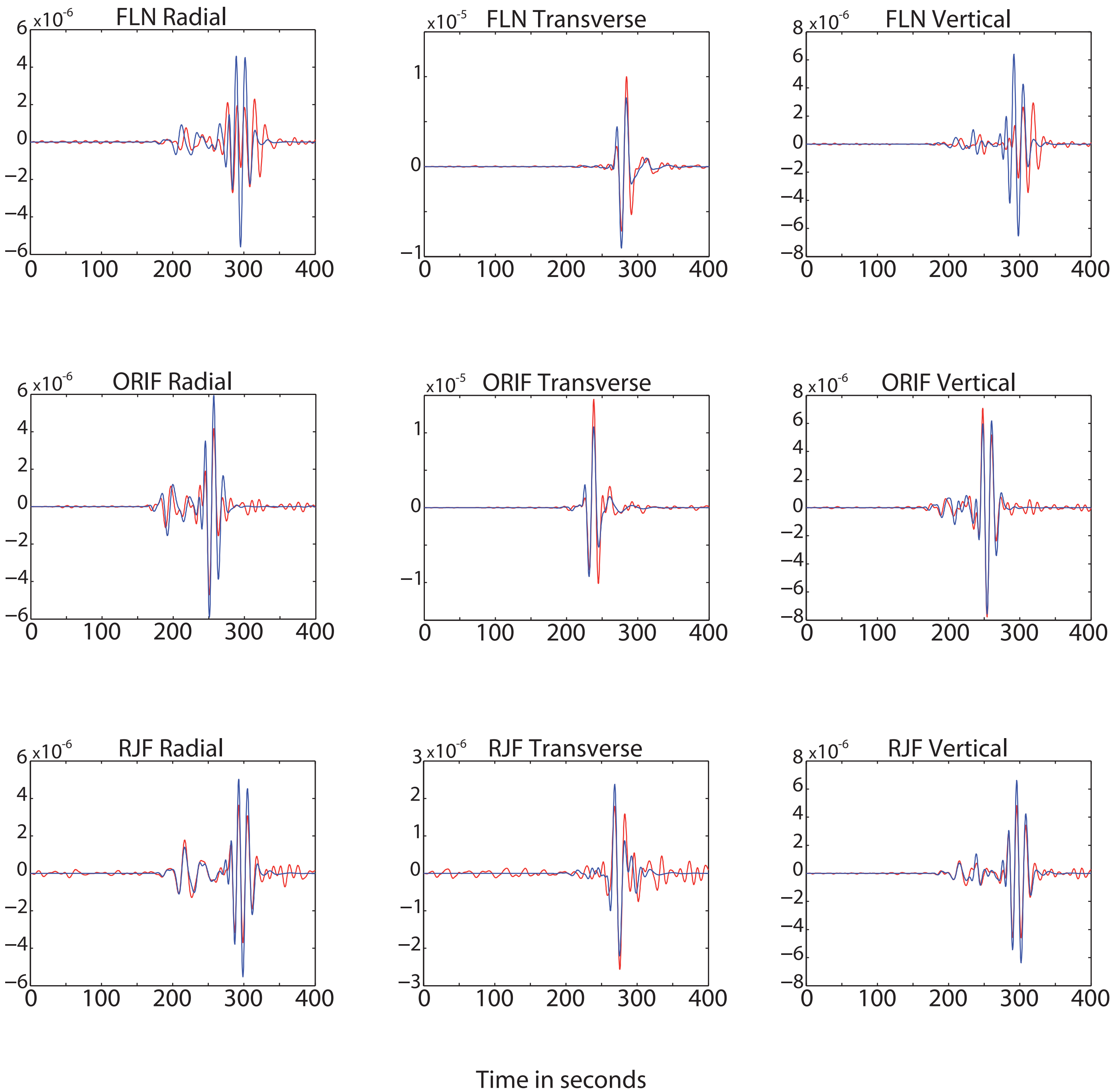

FLN Radial
FLN Transverse
FLN Vertical
ORIF Radial
ORIF Transverse
ORIF Vertical
RJF Radial
RJF Transverse
RJF Vertical
x10^-6
x10^-5
0
100
200
300
400
Time in seconds

Figure 2b

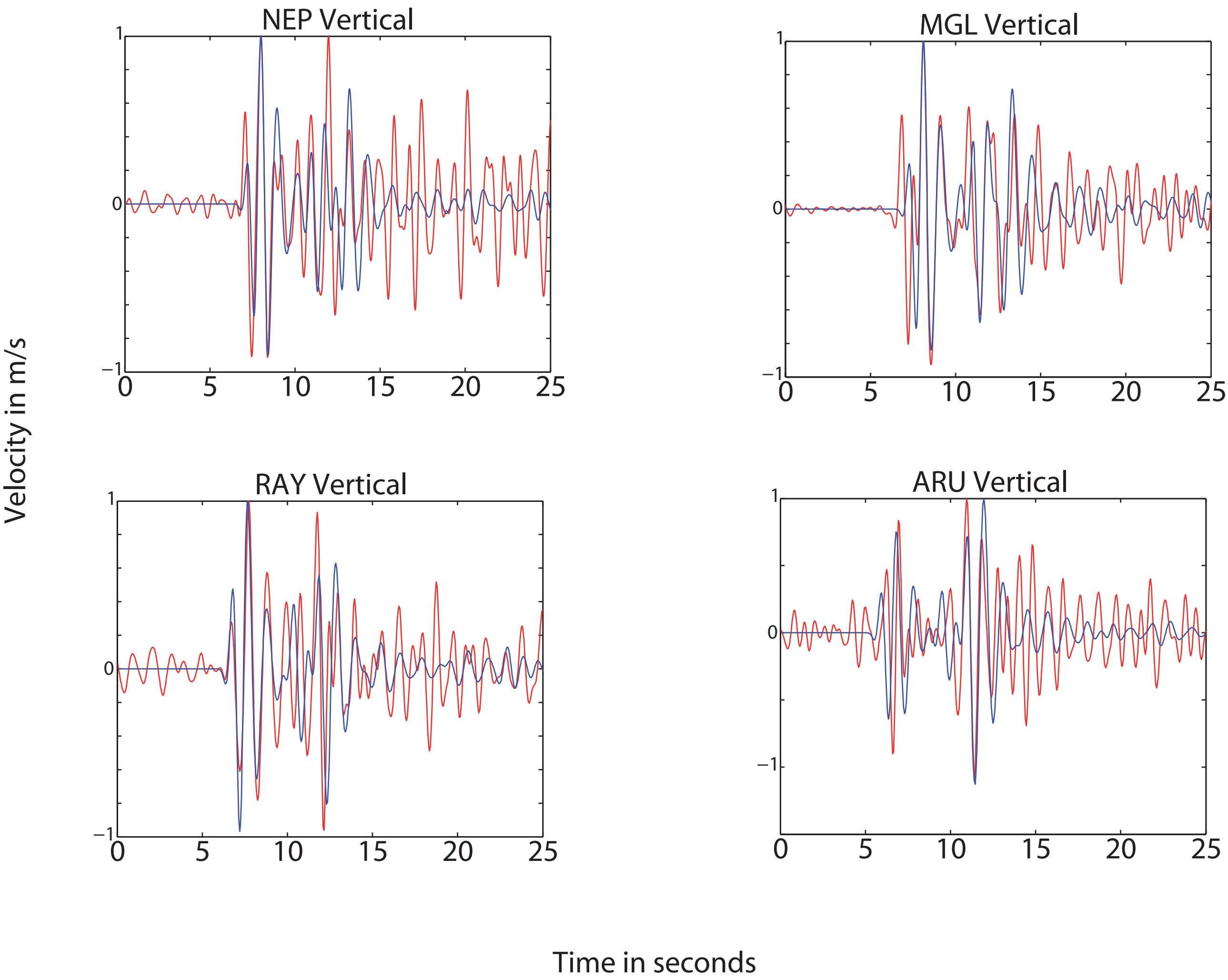

NEP Vertical
MGL Vertical
RAY Vertical
ARU Vertical
Velocity in m/s
Time in seconds
1
0
−1
0
5
10
15
20
25

Figure 2c

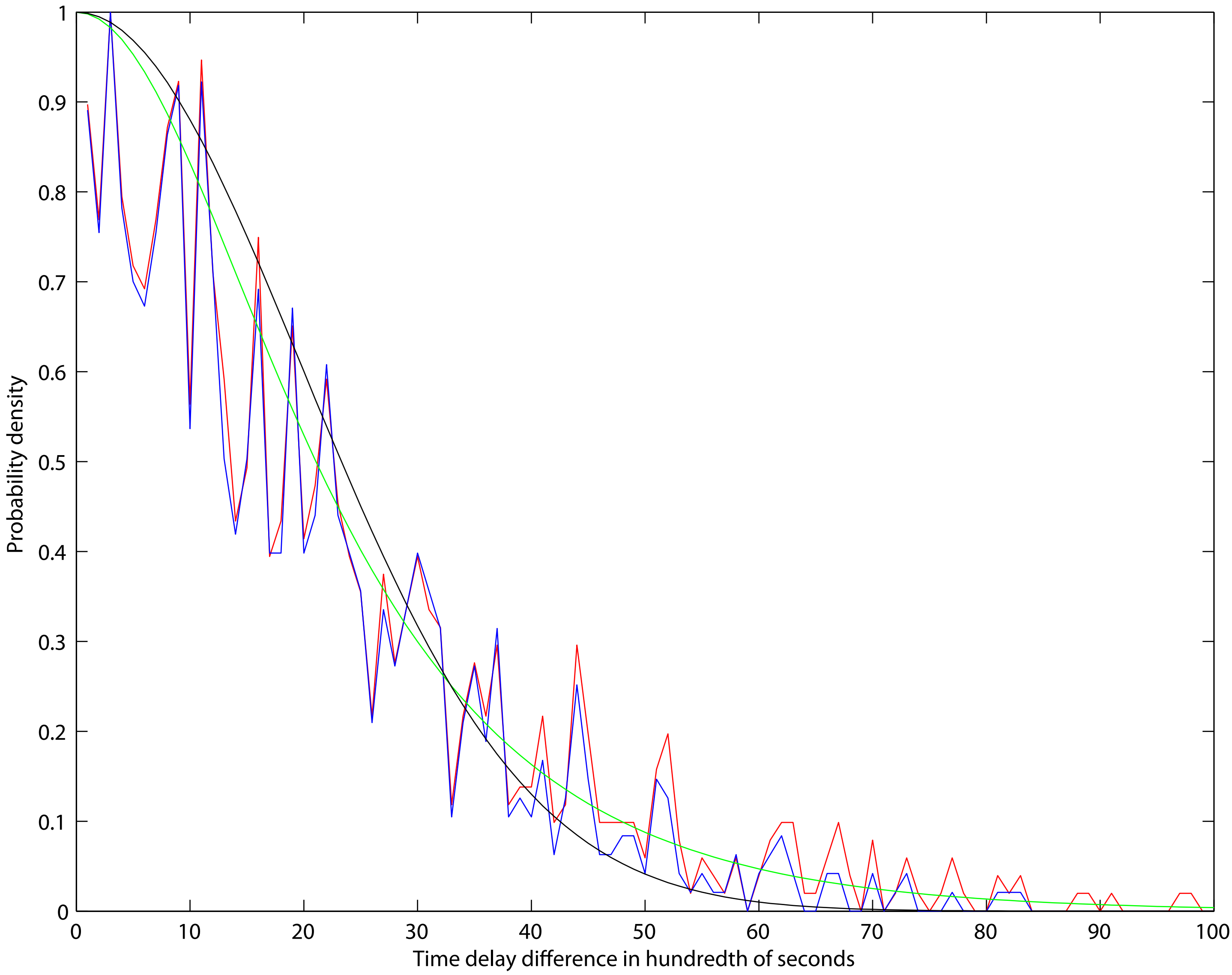

Probability density
Time delay difference in hundredth of seconds
0
0.1
0.2
0.3
0.4
0.5
0.6
0.7
0.8
0.9
1
10
20
30
40
50
60
70
80
90
100

Figure 3a

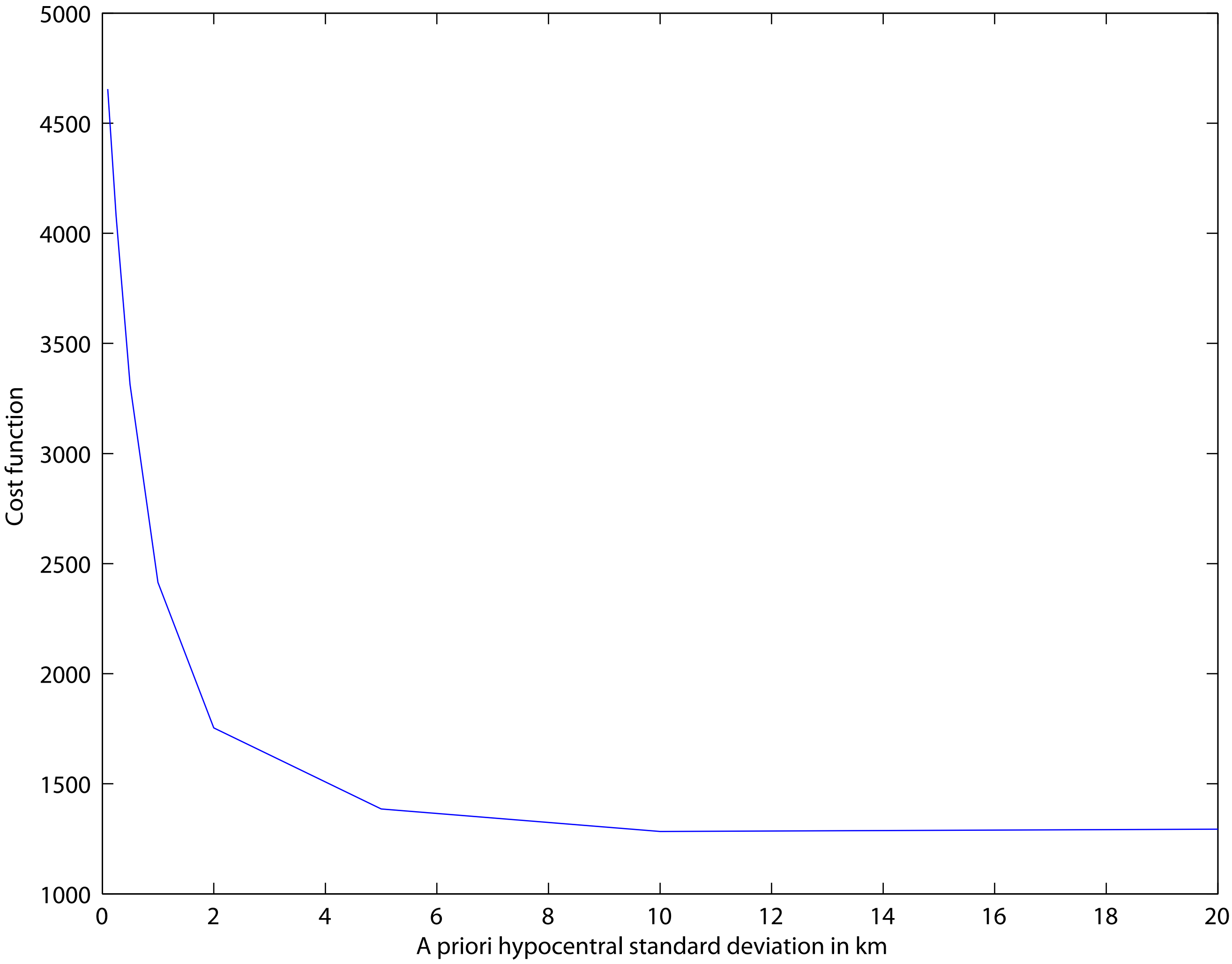
5000
4500
4000
3500
3000
2500
2000
1500
1000
Cost function
0
2
4
6
8
10
12
14
16
18
20
A priori hypocentral standard deviation in km

Figure 3b

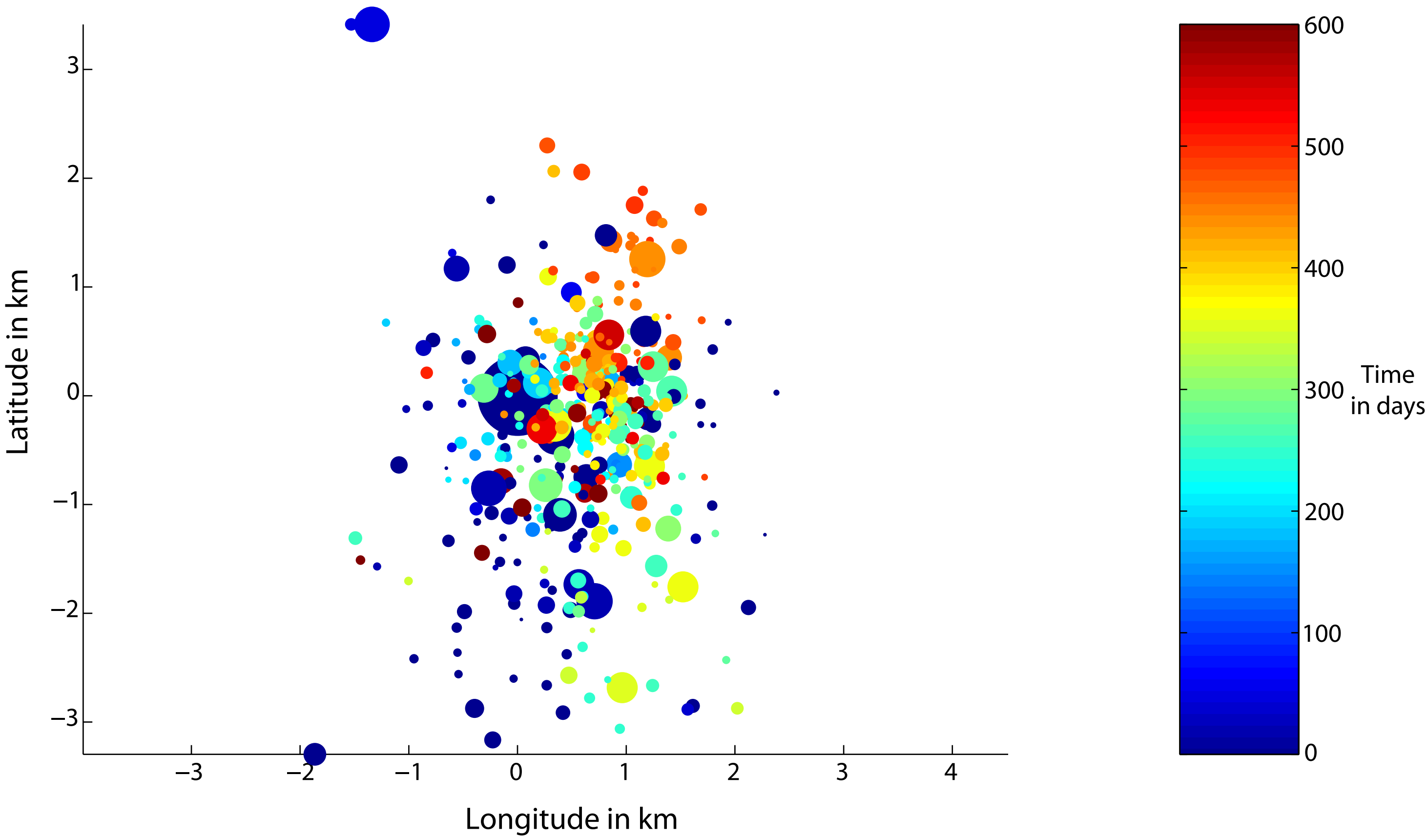

Latitude in km
Longitude in km
3
2
1
0
−1
−2
−3
−3
−2
−1
0
1
2
3
4
600
500
400
300
200
100
0
Time
in days

Figure 4a

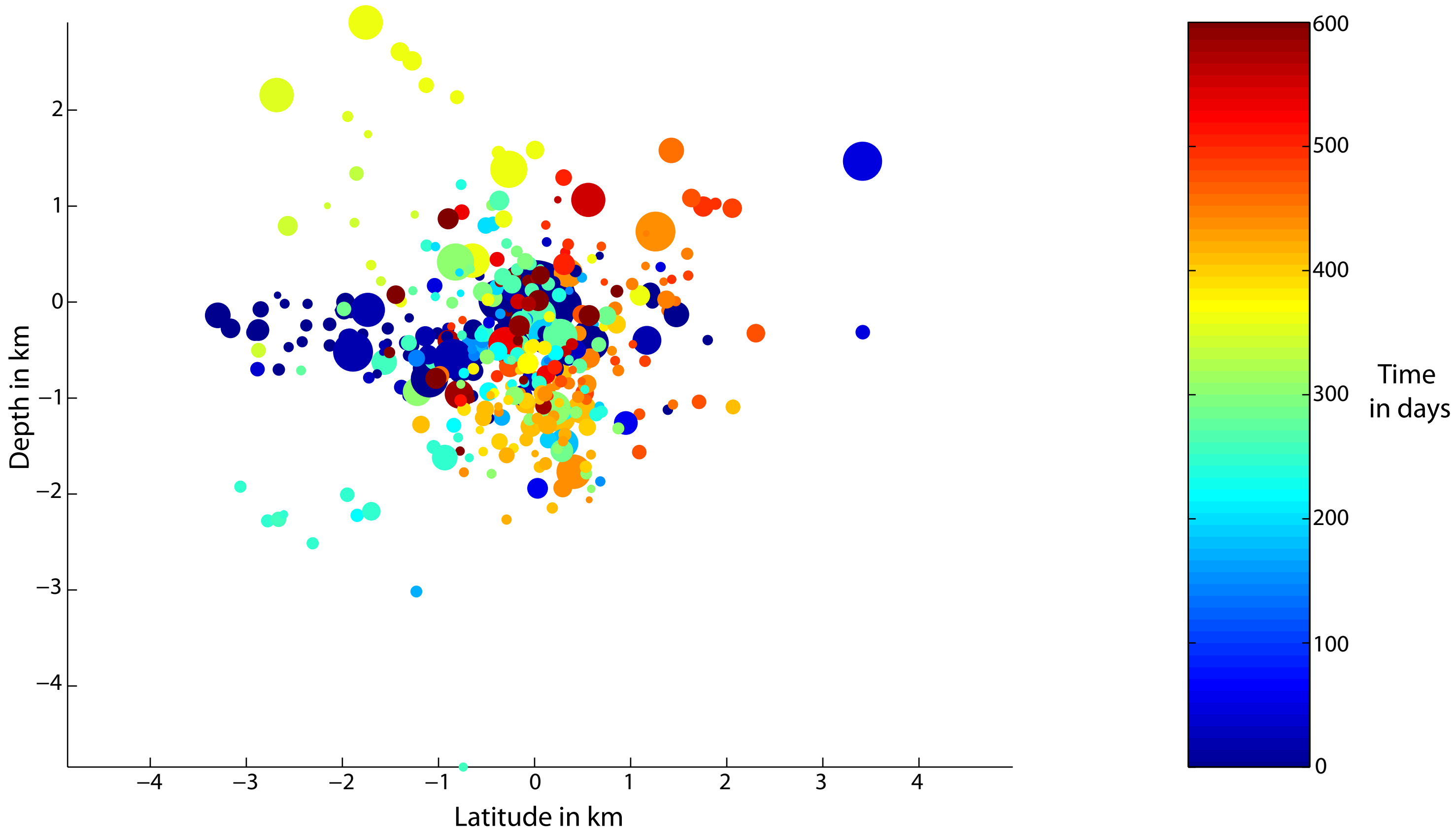

Figure 4b

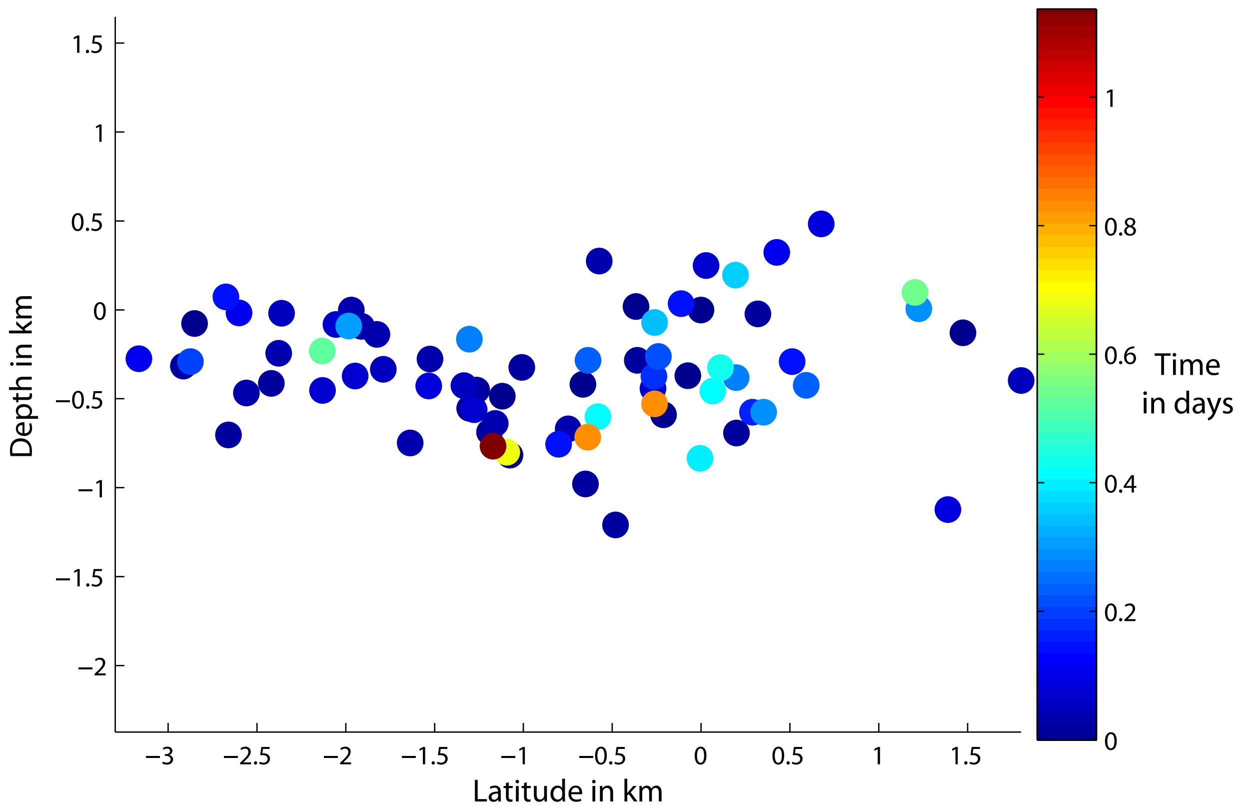
1.5
1
0.5
0
−0.5
−1
−1.5
−2
Depth in km
−3
−2.5
−2
−1.5
−1
−0.5
0
0.5
1
1.5
Latitude in km
1
0.8
0.6
0.4
0.2
0
Time
in days

Figure 4c

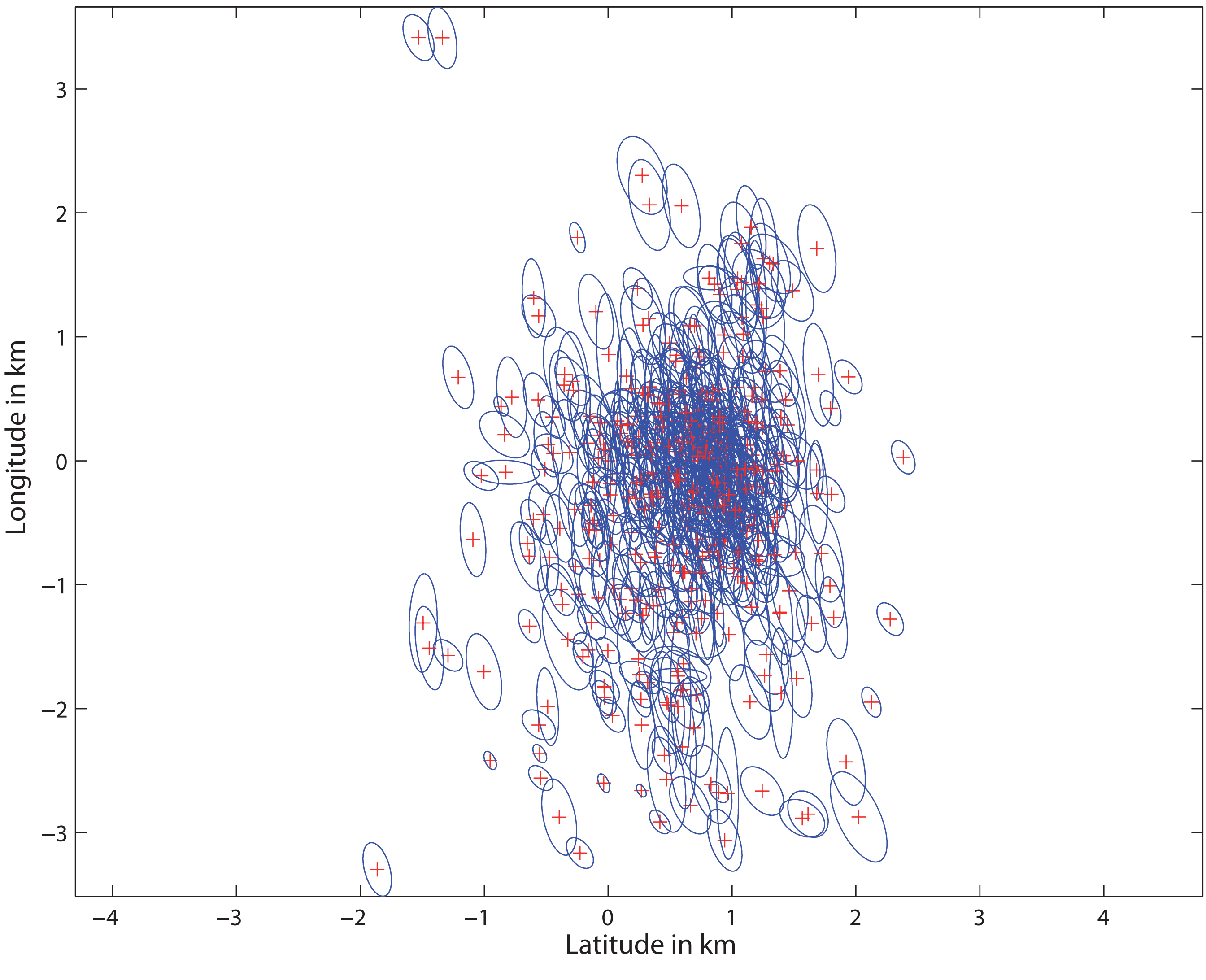

Figure 4d

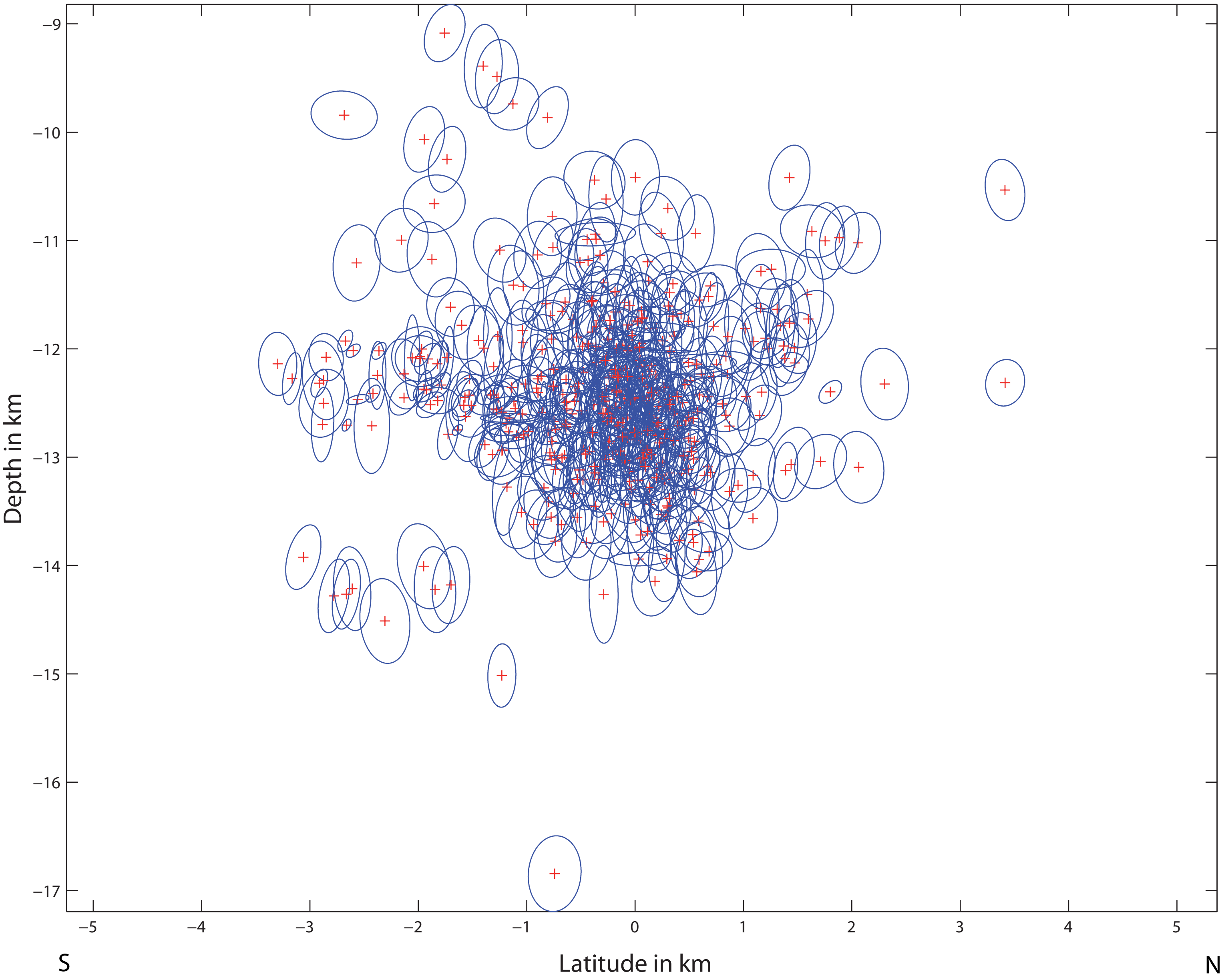
Depth in km
−9
−10
−11
−12
−13
−14
−15
−16
−17
−5
−4
−3
−2
−1
0
1
2
3
4
5
S
Latitude in km
N

Figure4e

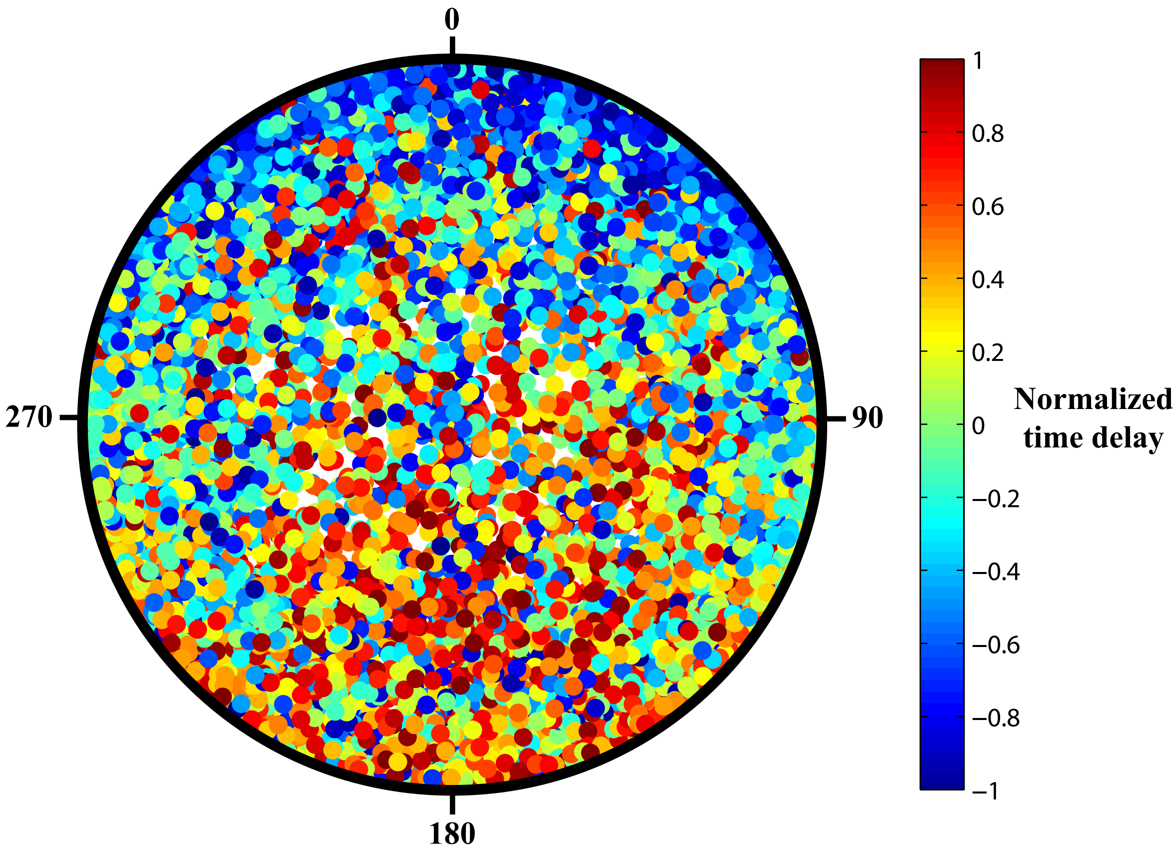

Figure 5a

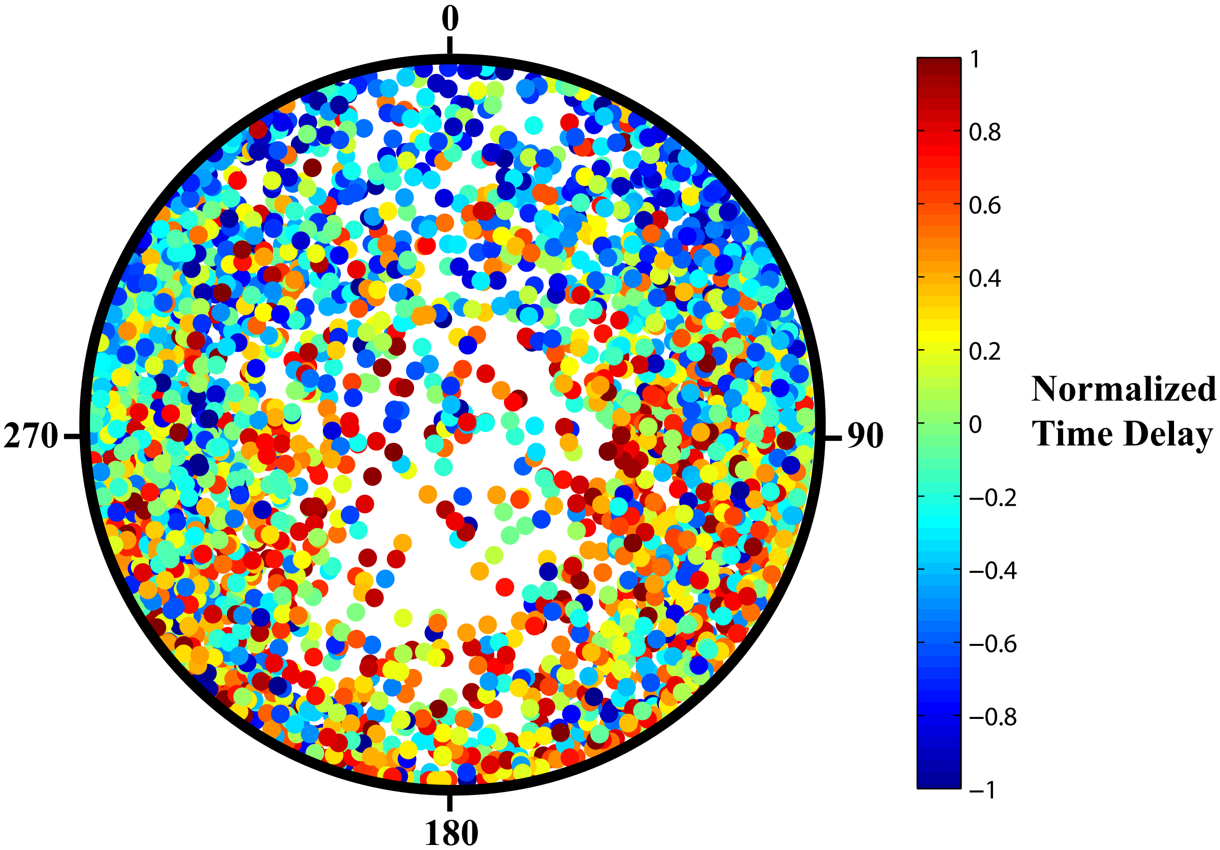

Figure 5b

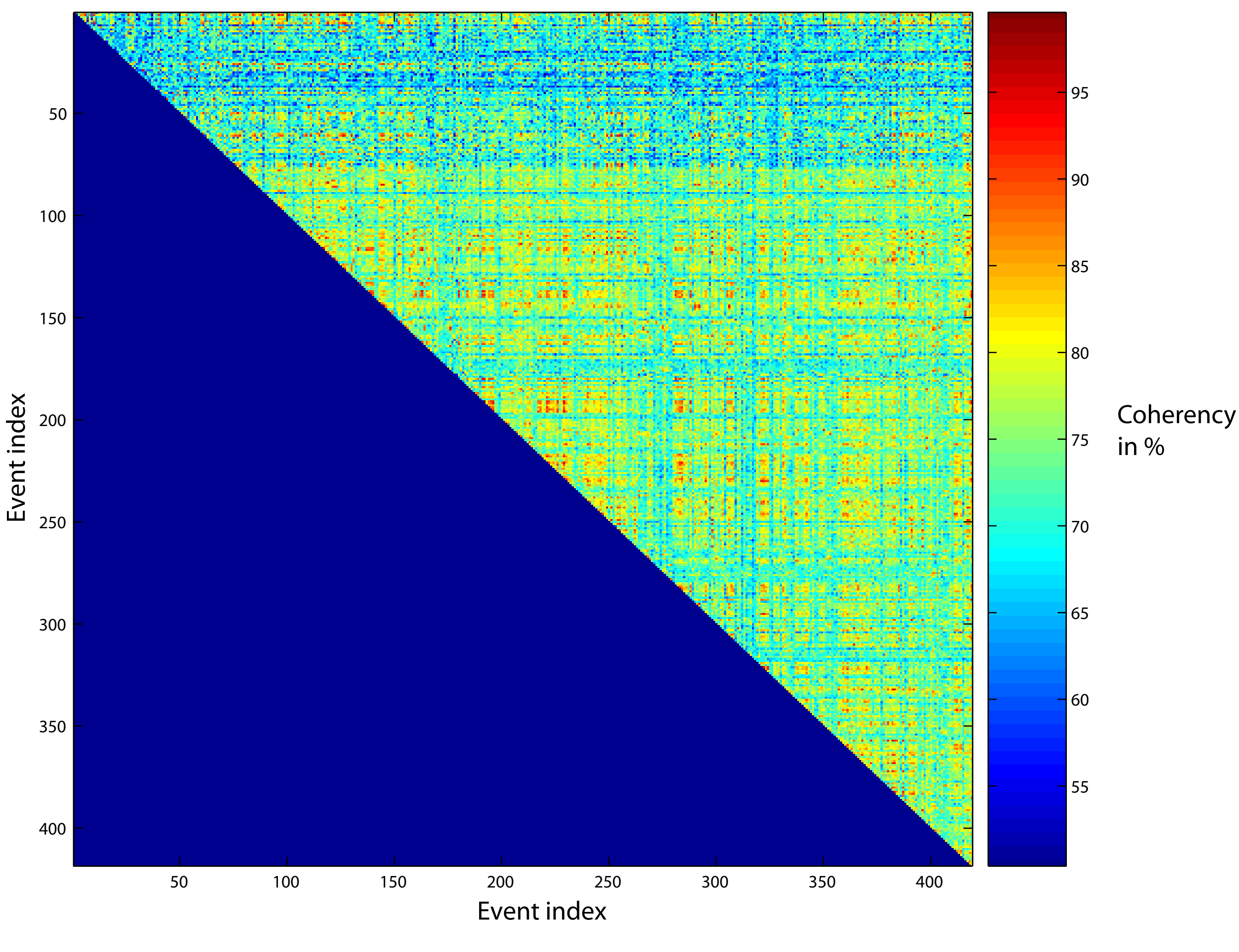

Event index
50
100
150
200
250
300
350
400
Event index
50
100
150
200
250
300
350
400
95
90
85
80
75
70
65
60
55
Coherency
in %

Figure 6

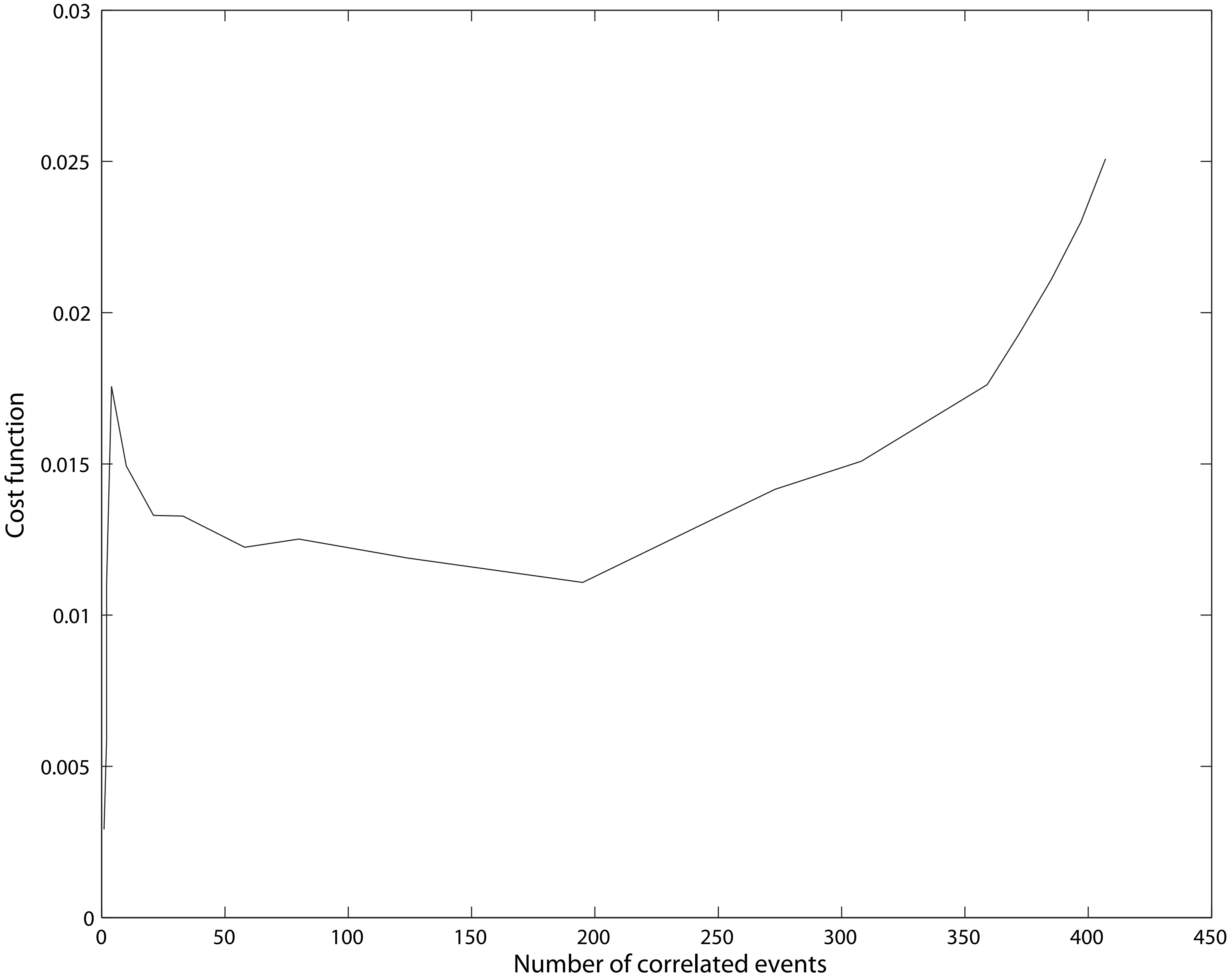
0.03
0.025
0.02
0.015
0.01
0.005
0
Cost function
0
50
100
150
200
250
300
350
400
450
Number of correlated events

Figure 7a

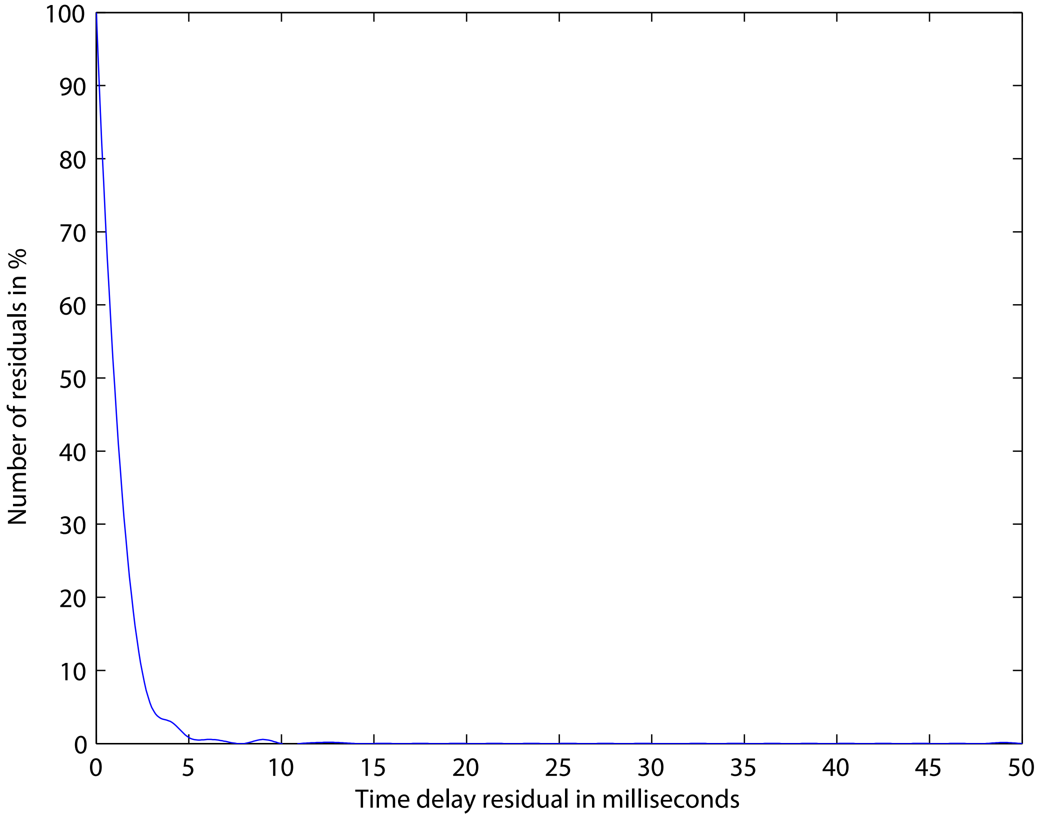
100
90
80
70
60
50
40
30
20
10
0
Number of residuals in %
0
5
10
15
20
25
30
35
40
45
50
Time delay residual in milliseconds

Figure 7b

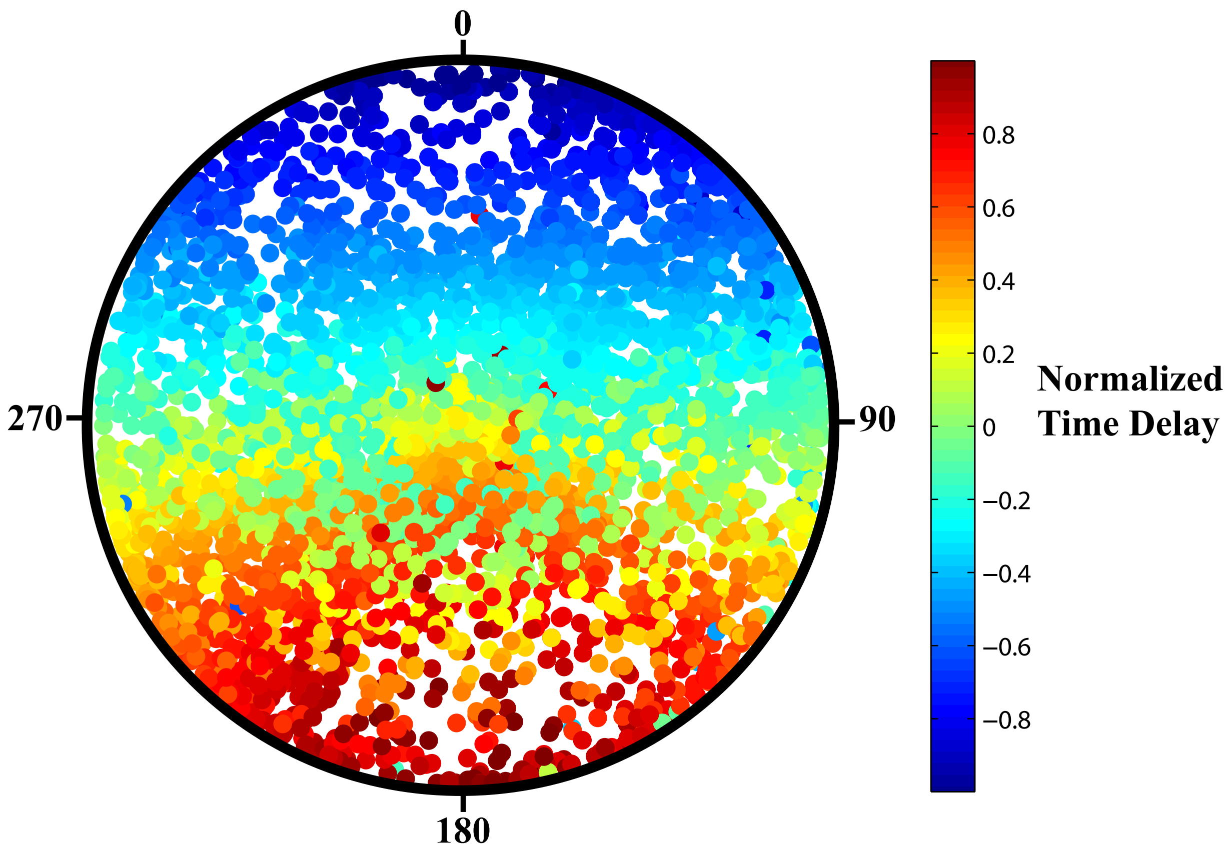

Figure 8

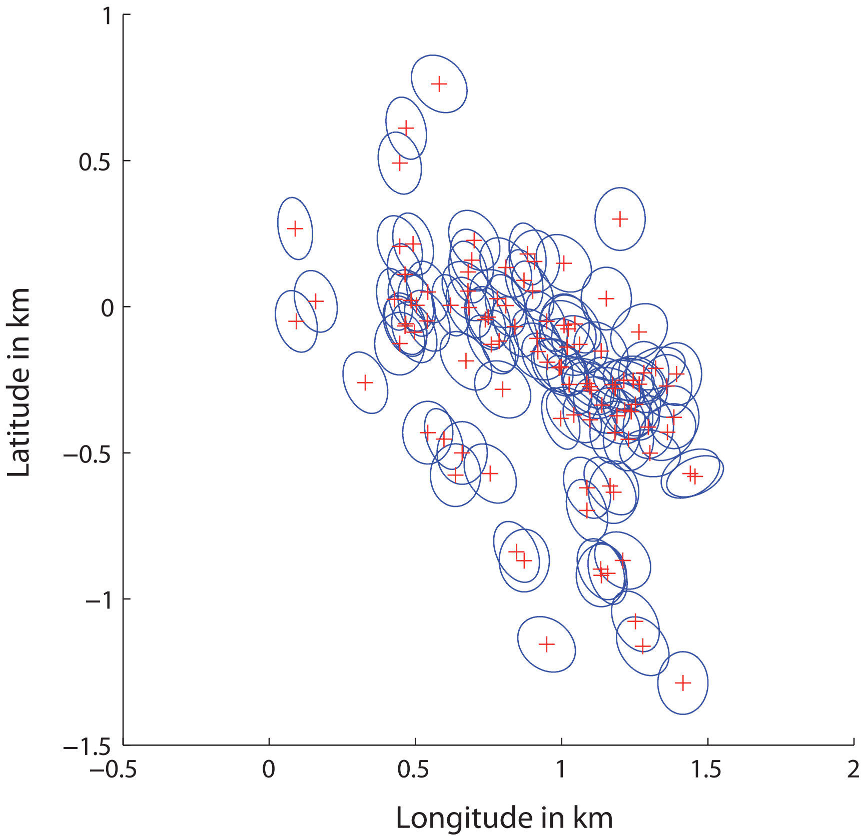

Figure 9a

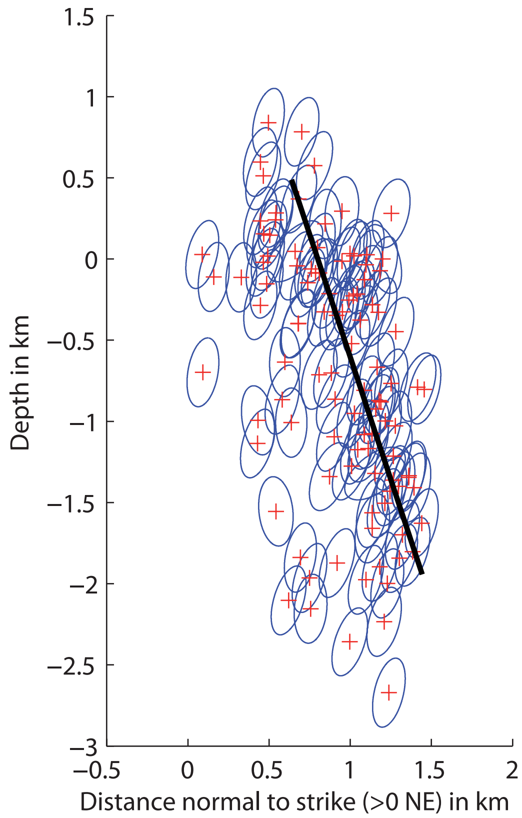

Depth in km
Distance normal to strike (>0 NE) in km
1.5
1
0.5
0
−0.5
−1
−1.5
−2
−2.5
−3
−0.5
0
0.5
1
1.5
2

Figure 9b

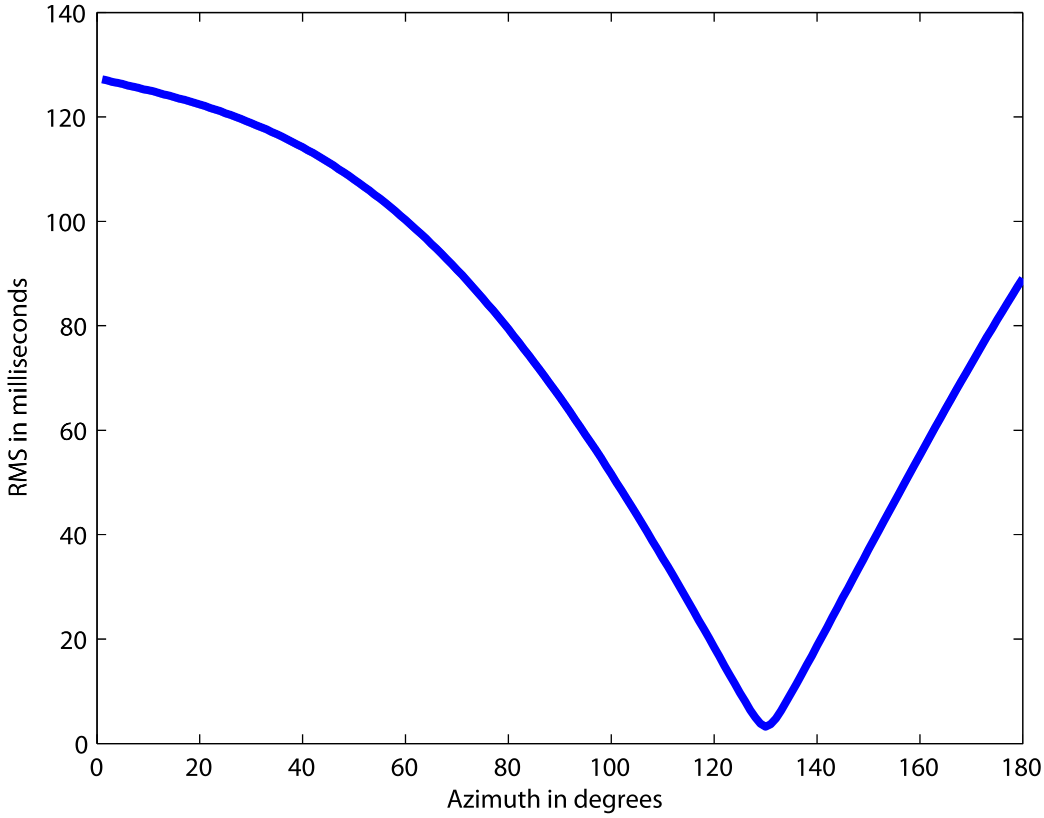

140
120
100
80
60
40
20
0
RMS in milliseconds
0
20
40
60
80
100
120
140
160
180
Azimuth in degrees

Figure 10a

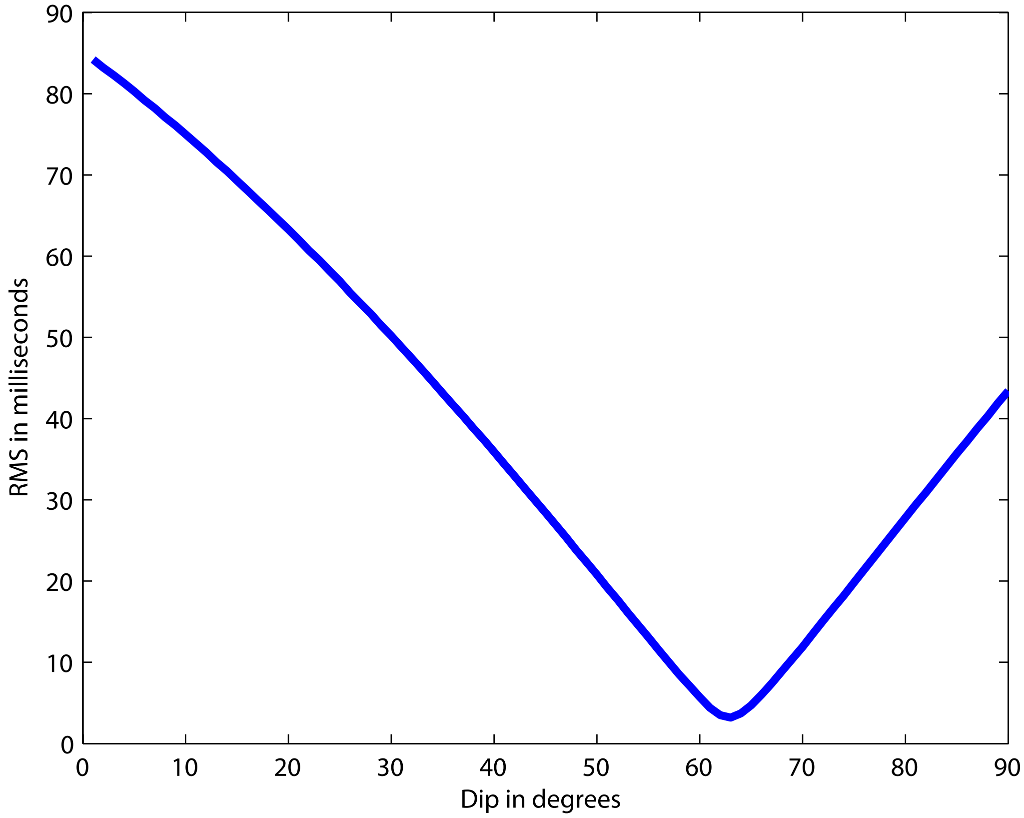

90
80
70
60
50
40
30
20
10
0
0
10
20
30
40
50
60
70
80
90
RMS in milliseconds
Dip in degrees

Figure 10b

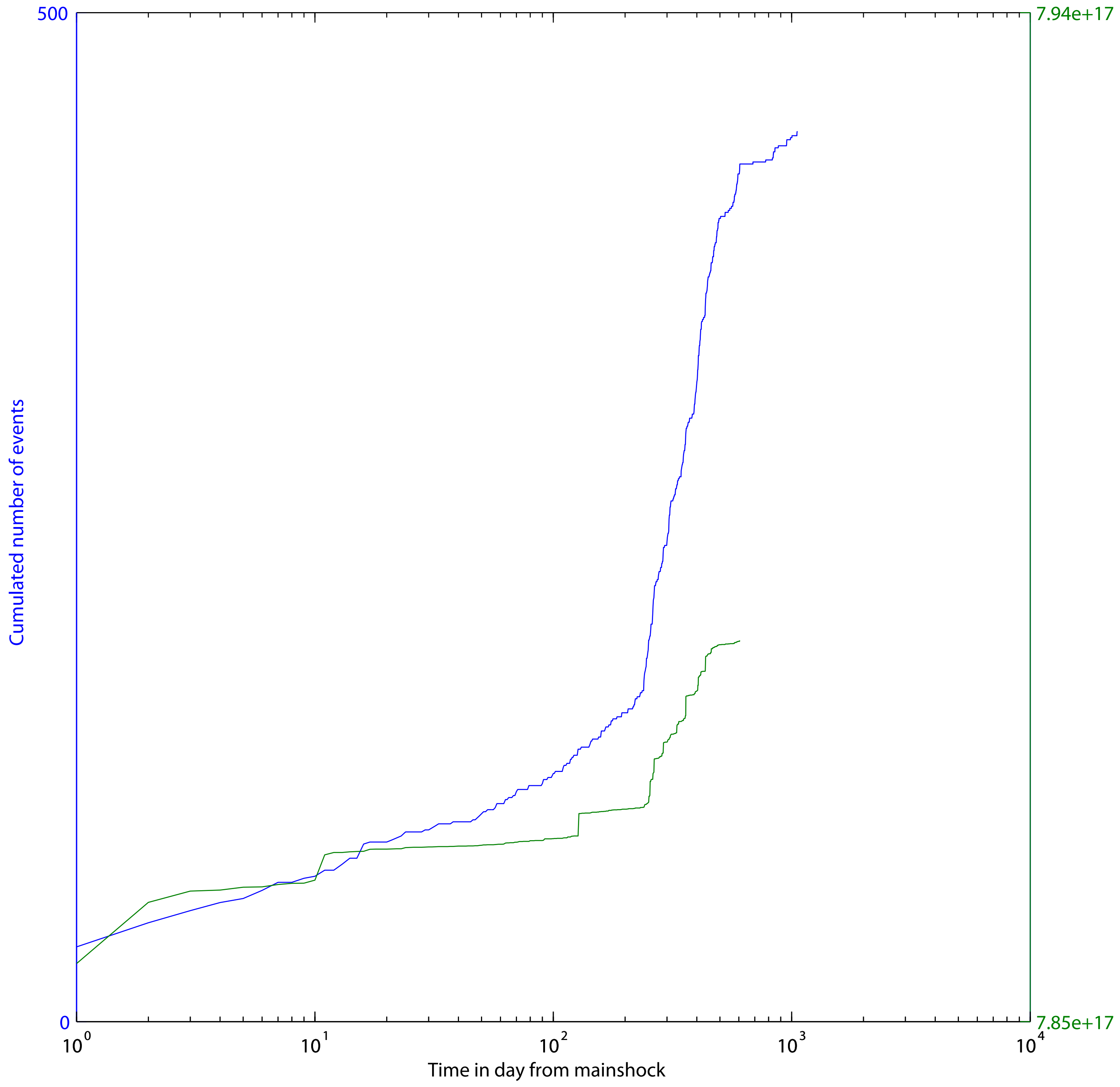
500
0
7.94e+17
7.85e+17
Cumulated number of events
Cumulative moment in N.m
10^0
10^1
10^2
10^3
10^4
Time in day from mainshock

Figure 11a

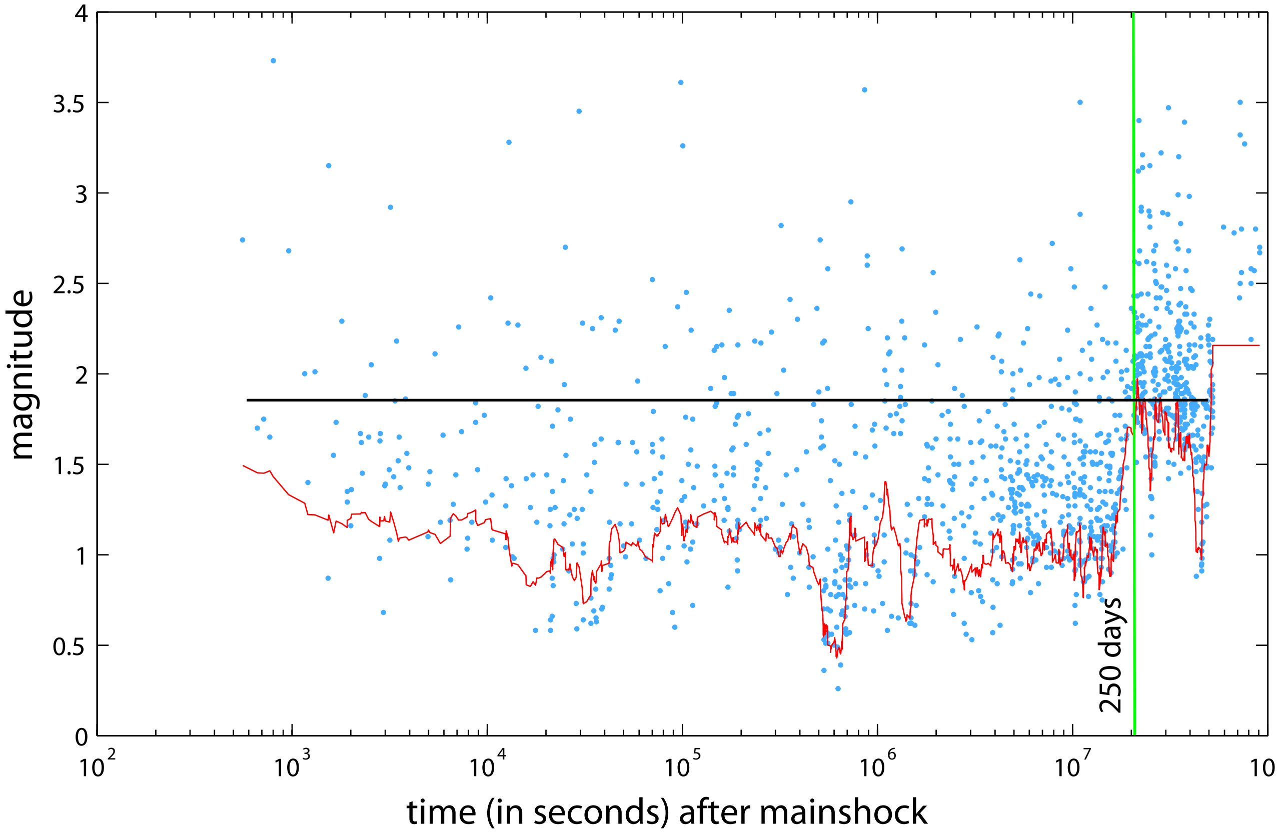

4
3.5
3
2.5
2
1.5
1
0.5
0
magnitude
250 days
10^2
10^3
10^4
10^5
10^6
10^7
10^8
time (in seconds) after mainshock

Figure 11b

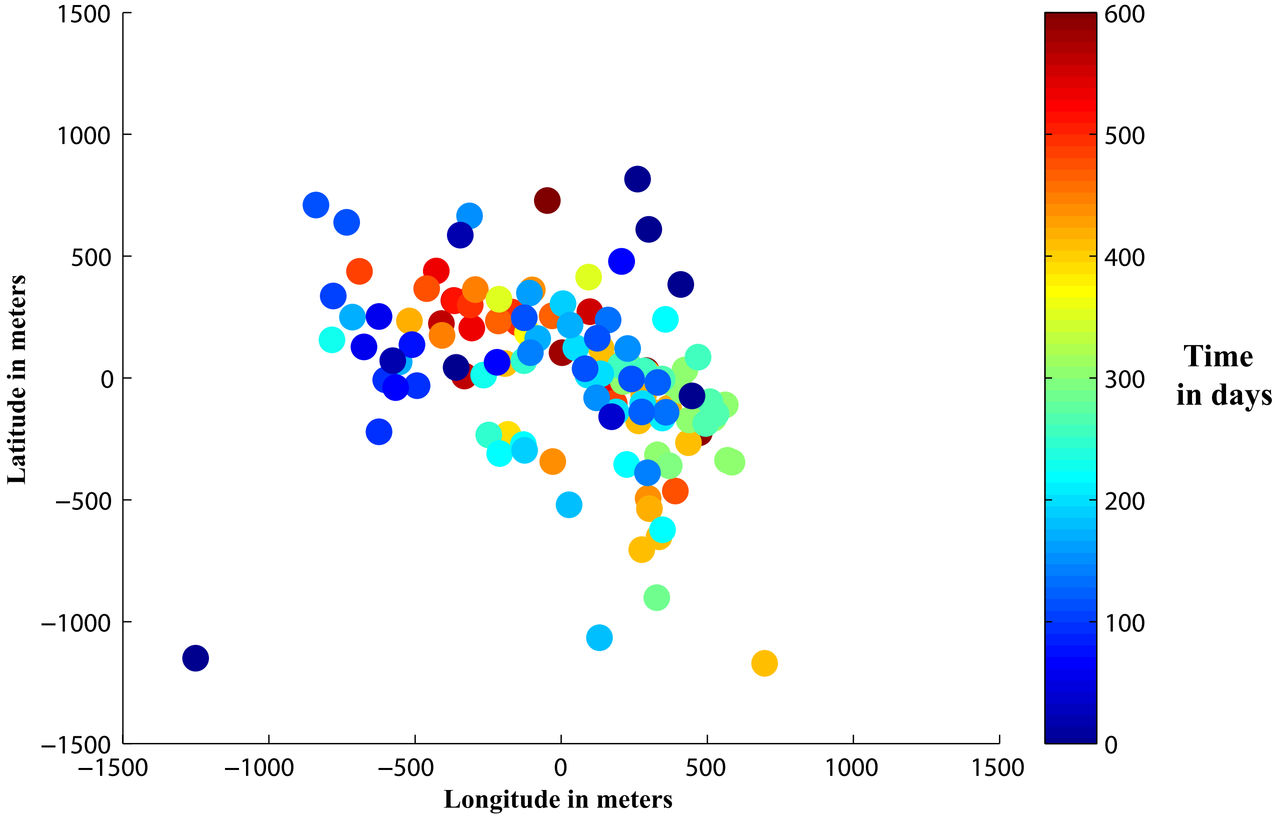
1500
1000
500
0
−500
−1000
−1500
Latitude in meters
−1500
−1000
−500
0
500
1000
1500
Longitude in meters
600
500
400
300
200
100
0
Time
in days

Figure 12a

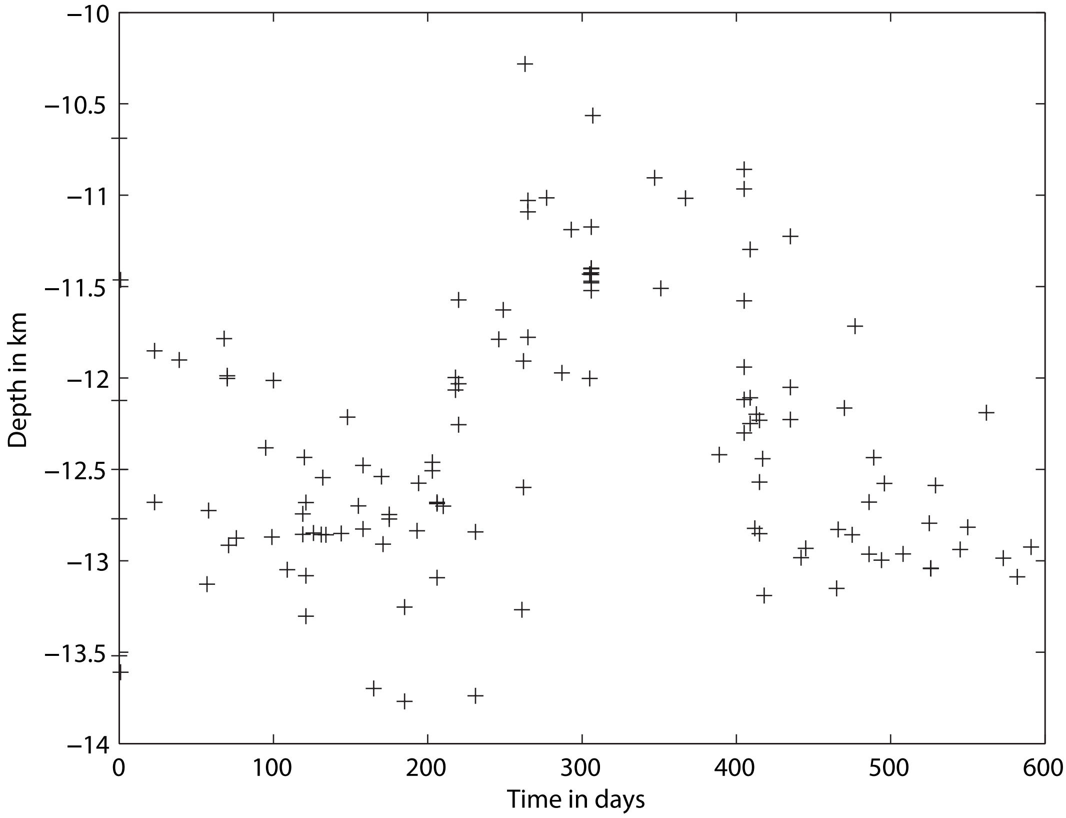
−10
−10.5
−11
−11.5
−12
−12.5
−13
−13.5
−14
Depth in km
0
100
200
300
400
500
600
Time in days

Figure 12b

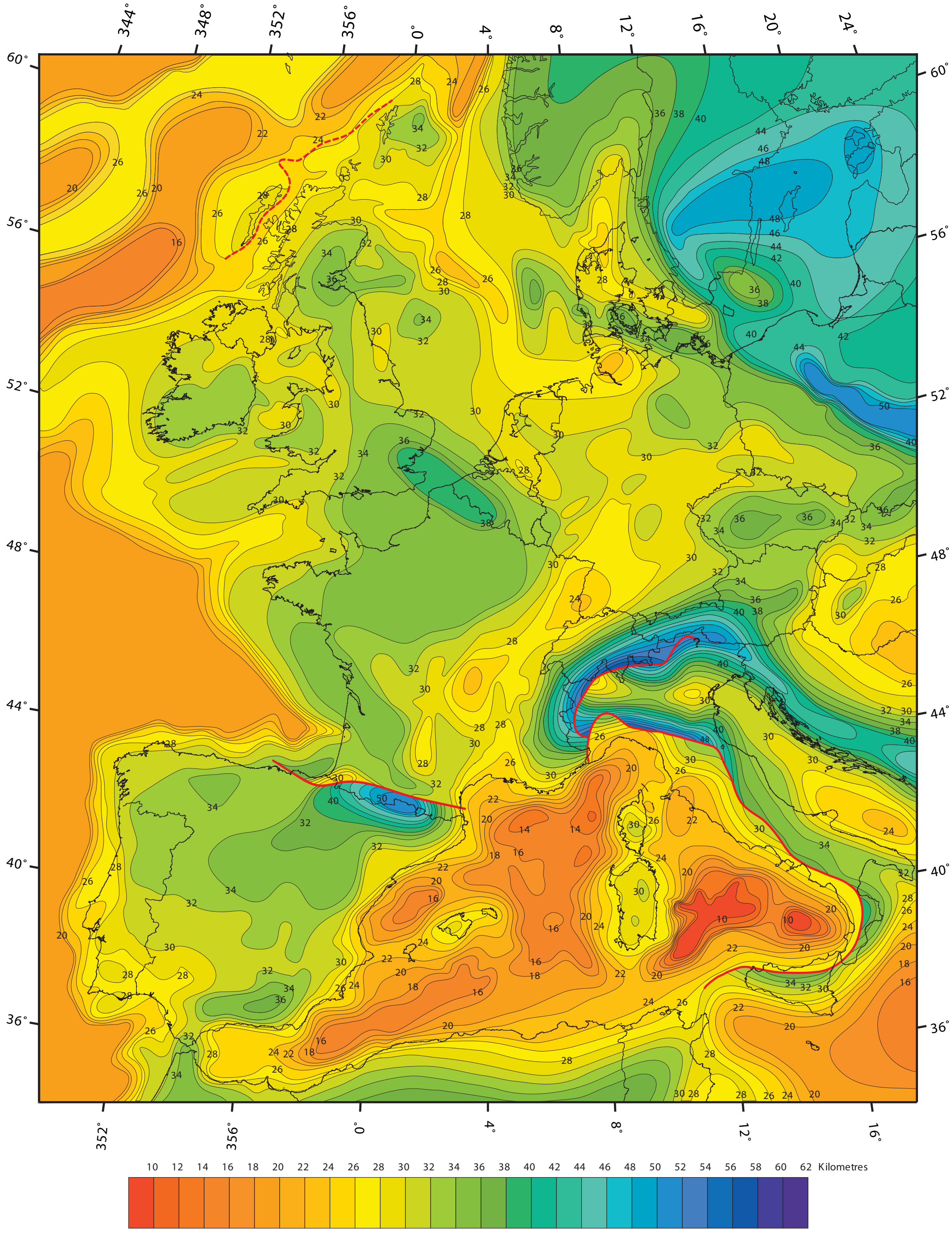

Projection: Lambert Azimuthal Equal Area; Centre: 04°.00''/48°.00''; Region : W/E/N/S = 350°/28°/62°/34°; Ellipsoide wgs-84

Moho depth in km

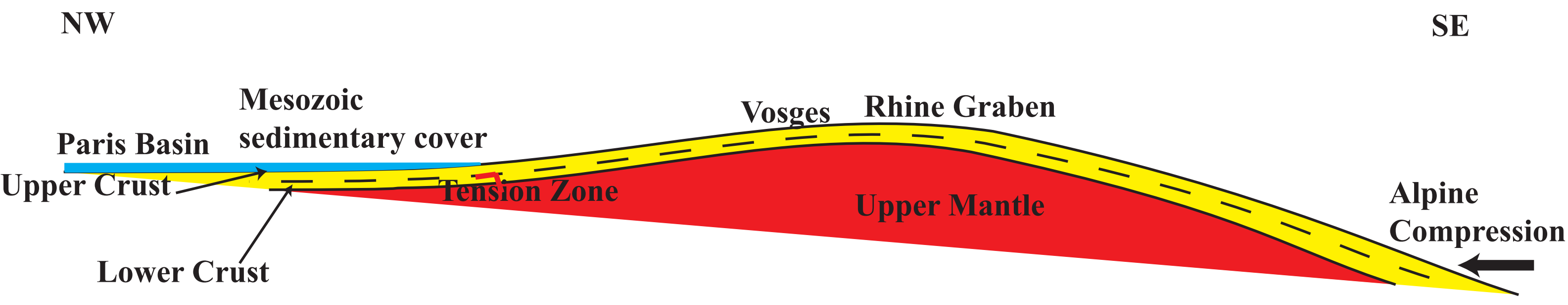
NW
SE
Mesozoic
sedimentary cover
Paris Basin
Upper Crust
Lower Crust
Vosges
Rhine Graben
Tension Zone
Upper Mantle
Alpine
Compression

Figure 13b